# Geometry of Freezing Impacts Ice Composition: Implications for Icy Satellites

Buffo Jacob[1], Meyer Colin R[1], Chivers Chase[2], Walker Catherine Colello[3], Huber Christian[4], and Schmidt Britney Elyce[2]

[1]Dartmouth College
[2]Georgia Institute of Technology
[3]Woods Hole Oceanographic Institution
[4]Brown University

November 16, 2022

**Abstract**

Non-ice impurities within the ice shells of ocean worlds (e.g., Europa, Enceladus, Titan) are believed to play a fundamental role in their geophysics and habitability and may become a surface expression of subsurface ocean properties. Heterogeneous entrainment and distribution of impurities within planetary ice shells have been proposed as mechanisms that can drive ice shell overturn, generate diverse geological features, and facilitate ocean-surface material transport critical for maintaining a habitable subsurface ocean. However, current models of ice shell composition suggest that impurity rejection at the ice-ocean interface of thick contemporary ice shells will be exceptionally efficient, resulting in relatively pure, homogeneous ice. As such, additional mechanisms capable of facilitating enhanced and heterogeneous impurity entrainment are needed to reconcile the observed physicochemical diversity of planetary ice shells. Here we investigate the potential for hydrologic features within planetary ice shells (sills and basal fractures), and the unique freezing geometries they promote, to provide such a mechanism. By simulating the two-dimensional thermal and physicochemical evolution of these hydrological features as they solidify, we demonstrate that bottom-up solidification at sill floors and horizontal solidification at fracture walls generate distinct ice compositions and provide mechanisms for both enhanced and heterogeneous impurity entrainment. We compare our results with magmatic and metallurgic analogs that exhibit similar micro- and macroscale chemical zonation patterns during solidification. Our results suggest variations in ice-ocean/brine interface geometry could play a fundamental role in introducing compositional heterogeneities into planetary ice shells and cryoconcentrating impurities in (re)frozen hydrologic features.

# Geometry of Freezing Impacts Ice Composition: Implications for Icy Satellites

**J. J. Buffo[1], C. R. Meyer[1], C. J. Chivers[2, 3], C. C. Walker[3], C. Huber[4] and B. E. Schmidt[5]**
1 – Dartmouth College, 2 – Georgia Institute of Technology, 3 – Woods Hole Oceanographic Institution, 4 – Brown University, 5 – Cornell University

## Key Points

- When a brine freezes the direction of solidification affects the structure and composition of the resulting ice
- Ice formation at sill floors and fracture walls provide a mechanism for heterogeneous and amplified impurity entrainment in planetary ice shells
- Cryoconcentration of impurities in freezing intrashell hydrological features can impact ice shell material properties, geophysics, and habitability

## Abstract

Non-ice impurities within the ice shells of ocean worlds (e.g., Europa, Enceladus, Titan) are believed to play a fundamental role in their geophysics and habitability and may become a surface expression of subsurface ocean properties. Heterogeneous entrainment and distribution of impurities within planetary ice shells have been proposed as mechanisms that can drive ice shell overturn, generate diverse geological features, and facilitate ocean-surface material transport critical for maintaining a habitable subsurface ocean. However, current models of ice shell composition suggest that impurity rejection at the ice-ocean interface of thick contemporary ice shells will be exceptionally efficient, resulting in relatively pure, homogeneous ice. As such, additional mechanisms capable of facilitating enhanced and heterogeneous impurity entrainment are needed to reconcile the observed physicochemical diversity of planetary ice shells. Here we investigate the potential for hydrologic features within planetary ice shells (sills and basal fractures), and the unique freezing geometries they promote, to provide such a mechanism. By simulating the two-dimensional thermal and physicochemical evolution of these hydrological features as they solidify, we demonstrate that bottom-up solidification at sill floors and horizontal solidification at fracture walls generate distinct ice compositions and provide mechanisms for both enhanced and heterogeneous impurity entrainment. We compare our results with magmatic and metallurgic analogs that exhibit similar micro- and macroscale chemical zonation patterns during solidification. Our results suggest variations in ice-ocean/brine interface geometry could play a fundamental role in introducing compositional heterogeneities into planetary ice shells and cryoconcentrating impurities in (re)frozen hydrologic features.

## Plain Language Summary

The ice shells of ocean worlds are not pure water ice but contain significant amounts of salts and other ocean-derived impurities. These impurities are believed to play an important role in governing the material properties, evolution, and habitability of planetary ices. Furthermore, linking observations of impurity distributions on ice shell surfaces to interior properties and processes (e.g., ocean composition) is a fundamental pillar in our understanding of ice-ocean worlds. That said, material entrainment at the ice-ocean interfaces of thick ice shells will be inefficient, leading to relatively pure ice, and necessitating an explanation for how the compositional heterogeneities observed in ice shells are introduced. Here we explore a possible solution: the freezing of water bodies within ice shells that have solidification interfaces which propagate vertically upward (sill floors) and horizontally (fracture walls). We find that these solidification geometries facilitate enhanced and heterogeneous impurity entrainment. Our results suggest the solidification of saline water bodies within ice shells could play a key role in explaining the compositional diversity observed on ice-ocean world surfaces and that constraining the dynamics that govern these ice-brine systems will be critical in linking spacecraft measurements of planetary ice compositions to the properties of subsurface water reservoirs.

## 1. Introduction

Many high-priority ice-ocean worlds in our solar system possess geologically rich surfaces indicative of ongoing geophysical activity within their ice shells and potential ocean-surface interactions (e.g., fractures [*Craft et al.*, 2016; *Figueredo and Greeley*, 2004; *Nimmo and Schenk*, 2006; *Walker et al.*, 2014], plumes [*Matson et al.*, 2007; *Sparks et al.*, 2016; *Waite et al.*, 2006], chaos terrain [*Greenberg et al.*, 1999; *Schmidt et al.*, 2011], dilational bands [*Carr et al.*, 1998; *Fagents et al.*, 2000; *Howell and Pappalardo*, 2018; *Manga and Sinton*, 2004], cryohydrologic features [*Chivers et al.*, 2021; *Kalousová et al.*, 2014; *Manga and Michaut*, 2017; *Michaut and Manga*, 2014; *Quick et al.*, 2019]). Ongoing activity and associated material transport (e.g., [*Allu Peddinti and McNamara*, 2015; *Postberg et al.*, 2011]) have important implications for the geophysics [*Buffo et al.*, 2021b], habitability [*Vance et al.*, 2016; *Vance et al.*, 2020], and remote observation [*Culha et al.*, 2020; *Kalousova et al.*, 2017; *Schroeder et al.*, 2016; *Trumbo et al.*, 2019] of ice-ocean worlds and suggests planetary ice shells exhibit a wide array of spatiotemporally variable activity levels and geodynamic processes. Advection and diffusion of energy and mass (e.g., heat, salt, and other ocean-derived material) will govern the dynamic evolution of planetary ice shells and any intrashell hydrologic/geophysical structures contained therein (e.g., lenses, dikes, sills, fractures, convection-conduction boundaries, compositional heterogeneities) [*Buffo et al.*, 2021b]. The thermochemical properties of planetary ice shells will influence a myriad of important material/environmental characteristics, including but not limited to phase structure [*Buffo et al.*, 2021a; *Buffo*, 2019; *Buffo et al.*, 2021b], rheology [*Durham et al.*, 2005; *McCarthy et al.*, 2011], dielectric properties [*Kalousova et al.*, 2017; *Moore*, 2000; *Schroeder et al.*, 2016], density [*Barr and McKinnon*, 2007; *Han and Showman*, 2005; *Kalousová et al.*, 2018; *Pappalardo and Barr*, 2004], water activity [*Buffo et al.*, 2022; *Fox-Powell et al.*, 2016; *Hallsworth et al.*, 2007], and melting point [*McCarthy et al.*, 2013; *McCarthy et al.*, 2011; *Toner et al.*, 2014]. The transport of ocean-derived reductants and surface-derived oxidants across ice shells (via fractures, plumes, subduction/subsumption, or solid-state convection) has been suggested as a mechanism that could facilitate disequilibrated ocean chemistries and support redox driven metabolism [*Allu Peddinti and McNamara*, 2015; *Vance et al.*, 2016; *Vance et al.*, 2020]. Our current and near future understanding of icy world interiors is fundamentally dependent on remote sensing measurements and our ability to relate these observations to internal dynamics and properties (e.g., inferring ocean composition/habitability, determining instrument detection limits, quantifying putative biosignature expression) [*Bryson et al.*, 2020; *Gleeson et al.*, 2012; *Kalousova et al.*, 2017; *Schmidt*, 2020; *Schmidt and Buffo*, 2017; *Schroeder et al.*, 2016].

A crucial, yet underconstrained feature broadly impacting nearly all characteristics, properties, and dynamics of planetary ice shells is their physicochemical heterogeneity [*Buffo et al., 2020; Buffo et al.*, 2021b; *Vance et al.*, 2020]. Numerous numerical models and theoretical studies implement vertical or lateral variations in ice shell porosity, chemistry, liquid fraction, and material properties to generate results consistent with several observed and inferred icy world geophysical processes (e.g., subduction/subsumption [*Johnson et al.*, 2017], solid state convection [*Han and Showman*, 2005], diapirism [*Pappalardo and Barr*, 2004], eutectic melting and the generation of perched hydrological features [*Schmidt et al.*, 2011], ocean-surface material transport [*Hesse et al.*, 2019; *Vance et al.*, 2020], liquid water stability [*Chivers et al.*, 2021], tectonic feature generation [*Howell and Pappalardo*, 2018]). Numerous studies have analogized the crucial role impurities play in terrestrial geophysics [*Buffo et al., 2020; Buffo*, 2019; *Buffo et al.*, 2021b; *Steefel et al.*, 2005] and the stratigraphies of many planetary ice shells are thought to mirror that of Earth's lithosphere-mantle system (i.e., a brittle ice lithosphere overriding a ductile ice mantle) [*Nimmo and Pappalardo*, 2016; *Sotin and Tobie*, 2004]. Other studies highlight the profound importance of planetary ice shell composition and phase structure to the performance and efficacy of mission instruments (e.g., ice penetrating radar) and the interpretation of their data products [*Kalousova et al.*, 2017; *Moore*, 2000; *Schroeder et al.*, 2016]. Consequently, authors have long emphasized the important role impurities and physicochemical heterogeneities likely play in the dynamics, evolution, and habitability of ice-ocean worlds. For example, in their commentary on *Buffo et al.* [*2020*], *Vance et al.* [2020] discuss at length the specific role of salts and other ocean-derived impurities in governing icy world surface geology, the geophysics of planetary ice shells composed of both ice Ih and high pressure ices, ocean world habitability, life detection, and spacecraft observation interpretation. Nevertheless, we are only beginning to place physically realistic constraints on the impurity content and physicochemical heterogeneity of planetary ices and ice shells [*Buffo et al.*, *2020; Buffo et al.*, 2021b; *Hammond et al.*, 2018].

A fundamental component in accurately simulating ocean- or brine-derived planetary ices is the ability to simulate the complex multiphase dynamics that occur at ice-ocean/brine interfaces [*Feltham et al.*, 2006; *Hunke et al.*, 2011]. Typically characterized by porous brine-saturated ice, these dynamic interfacial layers play a disproportionate role in governing heat and material transport between ice and liquid reservoirs, as the interstitial hydrology, thermodynamics, and geochemistry of these complex regions ultimately dictate the level of impurity entrainment in, and thus physicochemical composition of, the adjacent ice [*Buffo et al.*, *2020; Buffo*, 2019; *Buffo et al.*, 2021b; *Feltham et al.*, 2006; *Hunke et al.*, 2011]. This has been observed in both laboratory settings and naturally occurring ice-ocean/brine systems (e.g., sea ice, hypersaline lake ice) [*Cottier et al.*, 1999; *Cox and Weeks*, 1974; *Eicken*, 1992; *Nakawo and Sinha*, 1981; *Worster and Rees Jones*, 2015]. The physics of multiphase reactive transport theory have been shown to successfully capture the dynamics and evolution of ice-ocean and ice-brine systems and are a staple of the most accurate high-resolution sea ice models (e.g., [*Parkinson*, 2019; *Parkinson et al.*, 2020b; *Wells et al.*, 2019]). Accordingly, state of the art planetary ice models have adopted and integrated the physics of multiphase reactive transport theory, to varying degrees of complexity, into their architectures. *Buffo et al.* [*2020*] and *Hammond et al.* [2018] independently designed one-dimensional reactive transport models to simulate the first order physicochemical composition of the ice shells of Europa and Triton, respectively. Other studies (e.g., [*Kalousová and Sotin*, 2020; *Kalousová et al.*, 2018; *Kalousová et al.*, 2014; 2016; *Sotin et al.*, 2002]) have designed and/or employed one- and two-dimensional multiphase transport models to simulate the generation and flow of meltwater in icy satellite shells, however these models do not include impurities (e.g. salts). To our knowledge, there are currently only two models that simulate two-dimensional multiphase reactive transport processes in planetary ices, those of *Buffo et al.* [2021b] and *Hesse et al.* [2019], who simulate the 2D physicochemical evolution of solidifying planetary ice shells and oxidant delivery through Europa's ice shell via porosity waves, respectively. These two studies provide the first steps in realizing the likely complex, dynamic, and heterogenous nature of geophysically active planetary ice shells. Currently, however, both investigations have only explored simplified planar ice geometries subject to unidirectional temperature gradients (cold upper boundary, warm lower boundary), limiting our understanding to relatively idealized systems.

The need to reconcile multiphase reactive transport processes at ice-ocean/brine interfaces with the potentially complex geometry of geophysical structures within the ice shells of ocean worlds is exemplified by *Chivers et al.* [2021] who simulate the two-dimensional physical and thermochemical evolution of solidifying perched water lenses within Europa's ice shell. As the lenses freeze inward, they entrain salt heterogeneously, leaving behind a chemically complex structure that will have distinct and gradated material properties (melting point, dielectric signatures, density, rheology, etc.). This is due to variations in the thermal gradients experienced by different portions of the chamber's walls (larger thermal gradients entrain more salt) as well as the geometry of the system. *Chivers et al.* [2021] assume no interstitial brine drainage, and thus one hundred percent retention of salt, for chamber walls that are solidifying upward – consistent with the physics that govern the retention of buoyant melt in the multiphase roofs of terrestrial magma chambers [*Huppert*, 1990; *Worster et al.*, 1990]. While *Chivers et al.* [2021] have parameterized salt entrainment as a function of thermal gradient, and therefore do not simulate fluid transport explicitly, they highlight the immense importance geometry and heterogeneous structure within planetary ice shells will likely play in their geochemical and geophysical evolution. Moreover, their study emphasizes the need to constrain the dynamics of multiphase interfacial layers in thermally and geometrically complex ice-ocean/brine systems, as such environments could be associated with several high-priority geophysical features within planetary ice shells (e.g., lenses, sills, dikes, fracture walls, the ice-ocean interface) [*Buffo et al.*, 2021b] (Figure 1). Given the significant impact solidification geometry has on the interfacial multiphase reactive transport processes, resulting physicochemical structure, and material properties of analogous magmatic and metallurgic systems (e.g., chemical zonation in magmatic dikes, A- and V-segregate formation in alloy ingots) [*Campbell*, 2003; *Chistyakova and Latypov*, 2009; *Chistyakova and Latypov*, 2010; *Fowler*, 1987; *Li et al.*, 2014; *Mehrabian et al.*, 1970; *Steefel et al.*, 2005; *Worster et al.*, 1990], it stands to reason that comparable heterogeneities could significantly impact the composition, material properties, and ultimately dynamics of ocean/brine-derived planetary ices. This has fundamental implications for the geophysics, geology, habitability, and remote investigation of ice-ocean worlds.

Here we extend the work of *Buffo et al.* [2021b] and present novel two-dimensional multiphase reactive transport simulations of two unique endmember geometries that may be present in the ice shells of ice-ocean worlds (sills and fractures). Additionally, we explore two distinct ocean chemistries (35 ppt [g/kg] sodium chloride (NaCl) and 35 ppt [g/kg] magnesium sulfate ($MgSO_4$)) and investigate model results over four orders of magnitude (simulation grid spacing ranging from 7.8125 x $10^{-3}$ m to 7.8125 m). The first geometry considers the bidirectional (top-down and bottom-up) solidification of an isolated sill intruded into the shallow ice shell of Europa (Figure 1). This allows us to validate the assumption of *Chivers et al.* [2021] – that bottom-up solidification will result in completex` retention of interstitial brine due to a lack of the gravitational instability that drives ice desalination (via brine drainage) during top-down solidification – by explicitly simulating the multiphase evolution of the system. Additionally, we compare the resulting vertical bulk salinity profiles and solidification times predicted using our model to those of *Chivers et al.* [2021] to constrain the predicted longevity of perched water features in Europa's shallow ice shell and the compositional fingerprint left by solidified intrusive features. The former provides an important constraint for astrobiological investigations and planetary protection protocols [*Schmidt*, 2020; *Schmidt and Buffo*, 2017]. The latter offers insight for interpreting ice penetrating radar measurements that depend on the physicochemical and dielectric properties of the ice shell [*Kalousova et al.*, 2017], such as those planned for Europa Clipper's REASON instrument and JUICE's RIME instrument [*Schroeder et al.*, 2016]. The second geometry we explore is the horizontal (edge to center) solidification of fluid filled basal fractures that extend upward into Europa's ice shell from the ice-ocean interface (Figure 1). We produce two-dimensional spatiotemporal maps of the physicochemical evolution of these solidifying fractures, compare their structural and compositional trends to magmatic and metal alloy analogs, and identify quantitative relationships between material entrainment and interfacial thermal gradients in this geometric configuration. We highlight the critical role interface geometry likely plays in the dynamics and properties of ice-ocean/brine systems, address the applicability and limitations of leveraging petrologic and metallurgic analogs to explain the dynamics of cryohydrologic systems, briefly describe collaborative opportunities between modelers and experimentalists that would target outstanding questions related to multiphase ice-ocean/brine systems, and discuss specific implications our results have for the geophysics, habitability, geology, observation, and ocean-surface material transport capabilities of planetary ice shells.

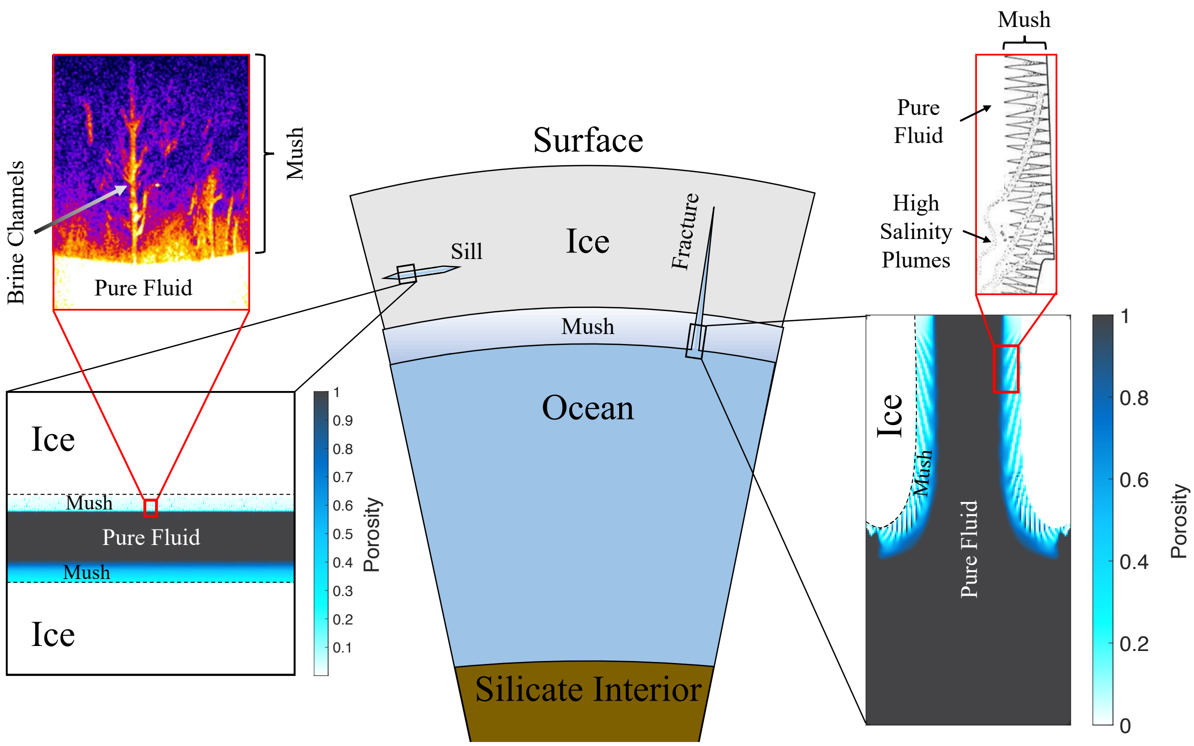


**Figure 1** – Hydrological features and multiphase interfaces in planetary ice shells. **Center)** Schematic representation of a typical ice Ih planetary ice shell and hydrological features that may populate its interior (fractures, sills). Modified from [*Buffo et al.*, 2021a]. **Left)** The multiphase interfaces that will likely characterize the roofs and floors of intruded/isolated water bodies within planetary ice shells. Bottom – Simulated porosity plot of a solidifying sill (Section 3.1); note the multiphase 'Mush' regions above and below the fluid filled center of the sill (domain is 1000 m by 1000 m, grid resolution = 7.8125 m). Top – Brine channels imaged in laboratory grown sea ice (modified from [*Worster and Rees Jones*, 2015]), demonstrating the fine scale structure associated with reactive transport (desalination) processes in top-down ice-ocean/brine solidification interfaces (image width is 3.7 cm). **Right)** The multiphase structure and dynamics of laterally freezing interfaces. Bottom – Simulated porosity plot of a basal fracture (Section 3.2); note the heterogenous mushy layers at the fracture sidewalls and sloped brine channels within the 'Mush' zone (domain is 1 m by 2 m). Top – Diagram depicting the formation of inclined channels in a laterally growing ice-brine mushy layer by dissolution of the solid ice crystal matrix by high salinity plumes (modified from [*Campbell*, 2003]), a process similar to that of A-segregate formation in metal alloys, See Figure 9).

## 2. Methods

To simulate the sill and fracture solidification scenarios described above we implement the two-dimensional multiphase reactive transport model SOFTBALL, first described in *Parkinson et al.* [2020b]. Capable of tracking the fluid dynamic, thermochemical, and phase evolution of binary alloy systems, SOFTBALL has been used by numerous studies to investigate the dynamics and properties of both terrestrial and planetary ices [*Buffo et al.*, 2021b; *Parkinson*, 2019; *Parkinson et al.*, 2020b; *Wells et al.*, 2019]. Here, we build on the work of *Buffo et al.* [2021b], who simulate the planar top-down solidification of planetary ice shells, to include more complex geometries and variable ocean chemistries.

In all simulations we begin with a static (fluid velocity = 0) completely fluid filled domain at a homogeneous temperature and salinity (Figure 2). Multidirectional solidification geometries (sills and basal fractures) are produced by prescribing undercooling to select boundaries (Figure 2). In the case of isolated sills these undercoolings are constant (Dirichlet) boundary conditions at the upper and lower boundaries, representative of a 1 km thick sill emplaced 1 km below the surface in a 5 km thick conductive ice lithosphere overlying a convective ice mantle (akin to the thermal environment implemented by *Chivers et al.* [2021]). Assuming a surface temperature of 100K, a brittle lithosphere to ductile mantle transition temperature of 260K, and a linear conductive thermal profile this results in sill roof temperatures of 132K and sill floor temperatures of 164K. During sill simulations we implement periodic boundary conditions at the horizontal edges of the domain. In the case of basal fractures, we implement constant (Dirichlet) undercoolings over the top halves of the horizontal boundaries (simulating the background ice-ocean interface across the domain's equatorial center). These undercoolings range from 200-260K to simulate fractures within a brittle ice lithosphere and a ductile mantle. The top boundary is set as a no flux (Neumann) no flow boundary condition for all transportable fields (mass, momentum, energy), while the bottom boundary is free to interact with an ambient underlying ocean.

To simulate variable ocean chemistries three key parameters were modified from those used by *Buffo et al.* [2021b]; the solutal contraction coefficient ($\beta$) describing how ocean/brine density changes with salt concentration, the eutectic concentration of the ocean ($C_e$) describing the concentration at which precipitation of solid salt/salt hydrates will occur, and the linear liquidus slope coefficient ($m$) describing the impact of salt on freezing point depression. In Table 1 we list the values we implement for these variables for both a NaCl ocean and a $MgSO_4$ ocean. All other variables utilized by SOFTBALL are the same as those used by *Buffo et al.* [2021b] (Table 1). We highlight the system of conservation equations solved by SOFTBALL in Figure 2 (mass, momentum, energy, and salt – closed using a salinity dependent linear phase relationship), but point the reader to *Parkinson et al.* [2020b] and *Buffo et al.* [2021b] for complete descriptions of SOFTBALL's functionality.

Lastly, to investigate the effects of simulation resolution on the resultant properties and structure of the solidified features, we ran simulations at several resolutions ranging from meter-scale fractures (grid resolution = 7.8125 x $10^{-3}$ m) to kilometer-scale fractures (grid resolution = 7.8125 m). A summary of all our simulations can be found in Table 2.

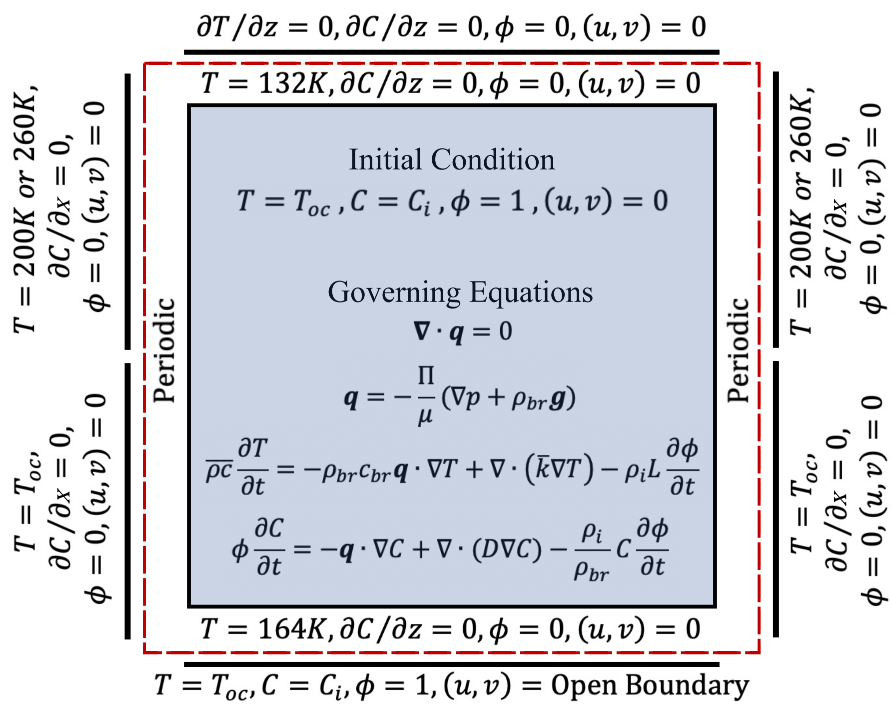


**Figure 2** – Governing equations, initial conditions, and boundary conditions during sill and fracture solidification simulations. Governing equations ensure conservation of mass, momentum (Darcy's Law), energy, and salt and are closed using a salinity dependent linear phase relationship to describe the liquidus and eutectic points of the system [*Buffo et al.*, 2021b; *Parkinson et al.*, 2020b] (variables: $T, C, \phi, u, v$). Initial conditions describe a static fluid filled domain at ambient ocean temperature and salinity. Boundary conditions inside the red dashed line are those used during sill simulations, while those outside the red dashed line are those used during basal fracture simulations. (All variables, their definitions, and their values, if applicable, can be found in Table 1. Variables with overbars are volume averaged quantities (i.e., $\bar{k} = k_{br}\phi + k_i(1-\phi)$), where the subscripts *i* and *br* refer to ice and brine phases, respectively, and $\phi$ is porosity).

| Variable | Definition | Value (35 ppt NaCl) | Value (35 ppt $MgSO_4$) |
|---|---|---|---|
| $\boldsymbol{\beta}$ | Solutal contraction coefficient | 7.7E-4 kg ppt$^{-1}$ | 8.3E-4 kg ppt$^{-1}$ |
| $\boldsymbol{c}$ | Specific heat | $c_{br}\phi + c_i(1-\phi)$ | $c_{br}\phi + c_i(1-\phi)$ |
| $\boldsymbol{c_{br}}$ | Specific heat of the ocean | 3985 J kg$^{-1}$ K$^{-1}$ | 3985 J kg$^{-1}$ K$^{-1}$ |
| $\boldsymbol{c_i}$ | Specific heat of ice | 2000 J kg$^{-1}$ K$^{-1}$ | 2000 J kg$^{-1}$ K$^{-1}$ |
| $C$ | Brine concentration | Calculated | Calculated |
| $\boldsymbol{C_e}$ | Eutectic concentration | 230 ppt | 175 ppt |
| $\boldsymbol{C_i}$ | Ocean concentration | 35 ppt | 35 ppt |
| $\boldsymbol{D}$ | Salt diffusion coefficient | 2E-9 m$^2$ s$^{-1}$ | 2E-9 m$^2$ s$^{-1}$ |
| $\boldsymbol{g}$ | Gravity | 1.32 m s$^{-2}$ | 1.32 m s$^{-2}$ |
| $\boldsymbol{k}$ | Thermal conductivity | $k_{br}\phi + k_i(1-\phi)$ | $k_{br}\phi + k_i(1-\phi)$ |
| $\boldsymbol{k_{br}}$ | Ocean thermal conductivity | 0.6 W m$^{-1}$ K$^{-1}$ | 0.6 W m$^{-1}$ K$^{-1}$ |
| $\boldsymbol{k_i}$ | Ice thermal conductivity | 2.0 W m$^{-1}$ K$^{-1}$ | 2.0 W m$^{-1}$ K$^{-1}$ |
| $\boldsymbol{L}$ | Latent heat of fusion | 334774 J kg$^{-1}$ | 334774 J kg$^{-1}$ |
| $\boldsymbol{m}$ | Linear liquidus slope | 0.0913 K ppt$^{-1}$ | 0.0228 K ppt$^{-1}$ |
| $\boldsymbol{\mu}$ | Dynamic viscosity | 1.88E-3 Pa s | 1.88E-3 Pa s |

| | | | |
|---|---|---|---|
| $\boldsymbol{p}$ | Dynamic pressure | Calculated | Calculated |
| $\boldsymbol{\phi}$ | Porosity | Calculated | Calculated |
| $\boldsymbol{\Pi}$ | Permeability | See [*Buffo et al.*, 2021b] | See [*Buffo et al.*, 2021b] |
| $\boldsymbol{q}$ | Darcy velocity | (u,v) m $s^{-1}$ | (u,v) m $s^{-1}$ |
| $\boldsymbol{\rho}$ | Density | $\boldsymbol{\rho}_{br}\phi + \boldsymbol{\rho}_i(1-\phi)$ | $\boldsymbol{\rho}_{br}\phi + \boldsymbol{\rho}_i(1-\phi)$ |
| $\boldsymbol{\rho}_{br}$ | Brine density | 1000+1000$\beta C$ kg $m^{-3}$ | 1000+1000$\beta C$ kg $m^{-3}$ |
| $\boldsymbol{\rho}_i$ | Ice density | 917 kg $m^{-3}$ | 917 kg $m^{-3}$ |
| $\boldsymbol{t}$ | Time | Independent variable | Independent variable |
| $\boldsymbol{T}$ | Temperature | Calculated | Calculated |
| $\boldsymbol{T}_{oc}$ | Ocean Temperature | 273.15-$mC_i$+0.01 K | 273.15-$mC_i$+0.01 K |
| $\boldsymbol{u}$ | Horizontal Darcy velocity | Calculated | Calculated |
| $\boldsymbol{v}$ | Vertical Darcy velocity | Calculated | Calculated |
| $\boldsymbol{x}$ | Horizontal spatial coordinate | Independent variable | Independent variable |
| $\boldsymbol{z}$ | Vertical spatial coordinate | Independent variable | Independent variable |

**Table 1 –** Variables and values used throughout the manuscript.

| Run Type | Undercooling (K) | Ocean Chemistry | Domain Size (m) | Resolution (m) |
|---|---|---|---|---|
| Sill | Top: 132, Bottom: 164 | NaCl | 1000 x 1000 | 3.90625 |
| Sill | Top: 132, Bottom: 164 | $MgSO_4$ | 1000 x 1000 | 3.90625 |
| Fracture | 200 | NaCl | 1 x 2 | 7.8125E-3 |
| Fracture | 200 | NaCl | 10 x 40 | 7.8125E-2 |
| Fracture | 200 | NaCl | 100 x 400 | 7.8125E-1 |
| Fracture | 200 | NaCl | 500 x 2000 | 7.8125 |
| Fracture | 200 | $MgSO_4$ | 1 x 2 | 7.8125E-3 |
| Fracture | 200 | $MgSO_4$ | 10 x 40 | 7.8125E-2 |
| Fracture | 200 | $MgSO_4$ | 100 x 400 | 7.8125E-1 |
| Fracture | 200 | $MgSO_4$ | 500 x 2000 | 7.8125 |
| Fracture | 260 | NaCl | 500 x 2000 | 7.8125 |

**Table 2 –** Environmental conditions and model domain architecture for all the simulations carried out during this investigation.

## 3. Results

### 3.1 Sills

Isolated brine-filled sills and other perched water features (e.g., dikes, lenses, laccoliths) may be commonplace in the shells of icy satellites and could have significant geological and astrobiological implications [*Chivers et al.*, 2021; *Manga and Michaut*, 2017; *Michaut and Manga*, 2014; *Schmidt et al.*, 2011; *Walker and Schmidt*, 2015]. Near surface (<5 km deep) water features could be the progenitors of geologically young, depressed/disrupted surface terrain (e.g., chaos [*Postberg et al.*, 2011], lenticulae [*Chivers et al.*, 2021; *Manga and Sinton*, 2004; *Michaut and Manga*, 2014]) and any shallow water reservoirs (especially those potentially interacting with the surface) are of immense astrobiological interest in the lens of both planetary exploration and planetary protection [*Council*, 2012; *Schmidt and Buffo*, 2017]. The intrusive nature of these features facilitates the generation of multidirectional freezing fronts along their boundaries and, if they are isolated from the underlying ocean, the potential for unique geochemical processes (e.g., concentration, saturation). In the case of isolated sills, top-down freezing will occur from the roof, bottom-up freezing will occur from the floor, and the residual brine will become increasingly saline until it reaches its saturation limit and begins to precipitate a eutectic mixture of ice and solid salt hydrates. Here we simulate the thermal and physicochemical evolution (from initial intrusion to complete solidification) of 1 km thick sills emplaced 1 km below the surface in a 5 km thick brittle ice lithosphere whose initial chemical composition is 35 ppt NaCl (Figure 3a) and 35 ppt $MgSO_4$ (Figure 3b). The grid resolution of both simulations is 3.90625 m.

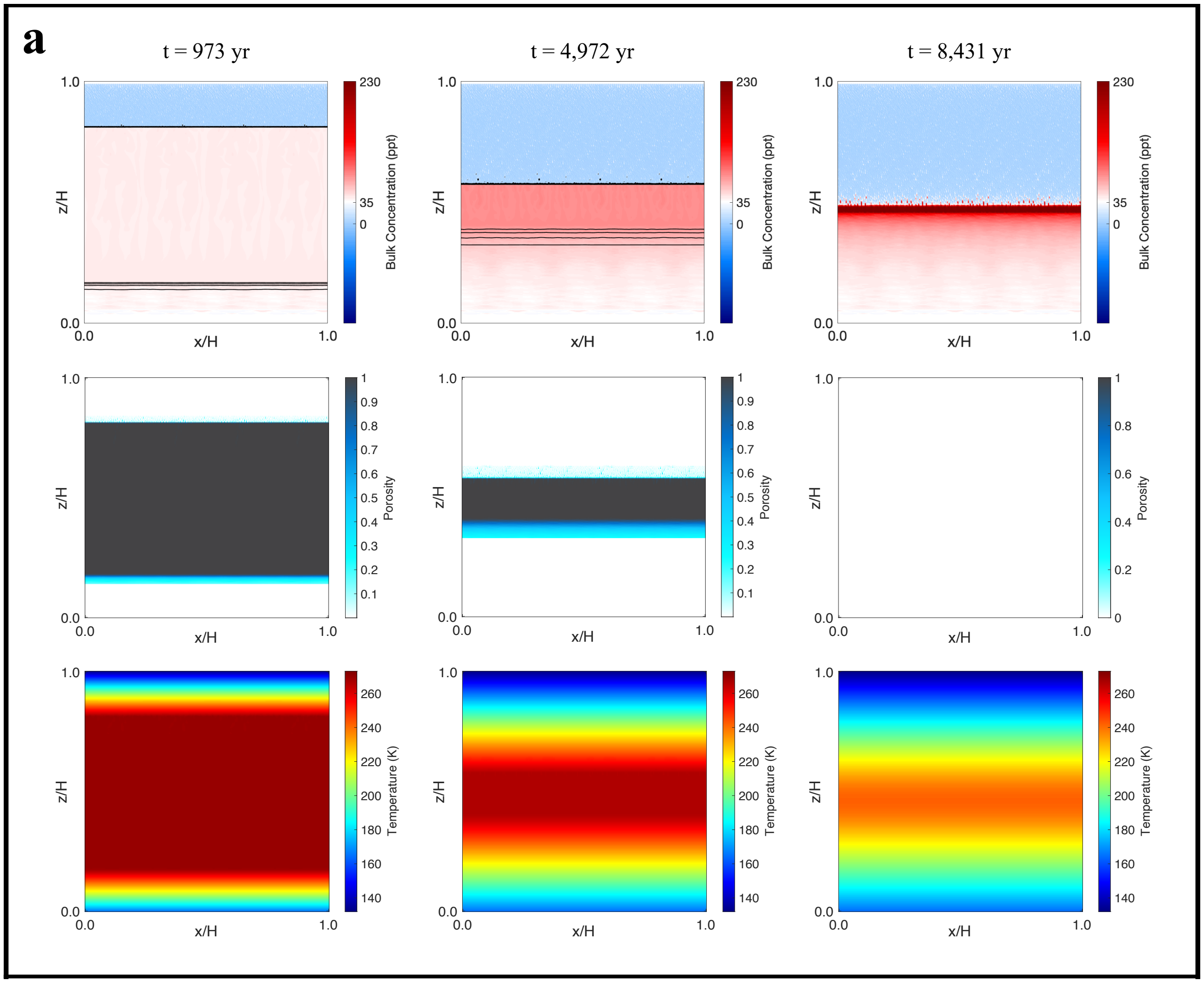

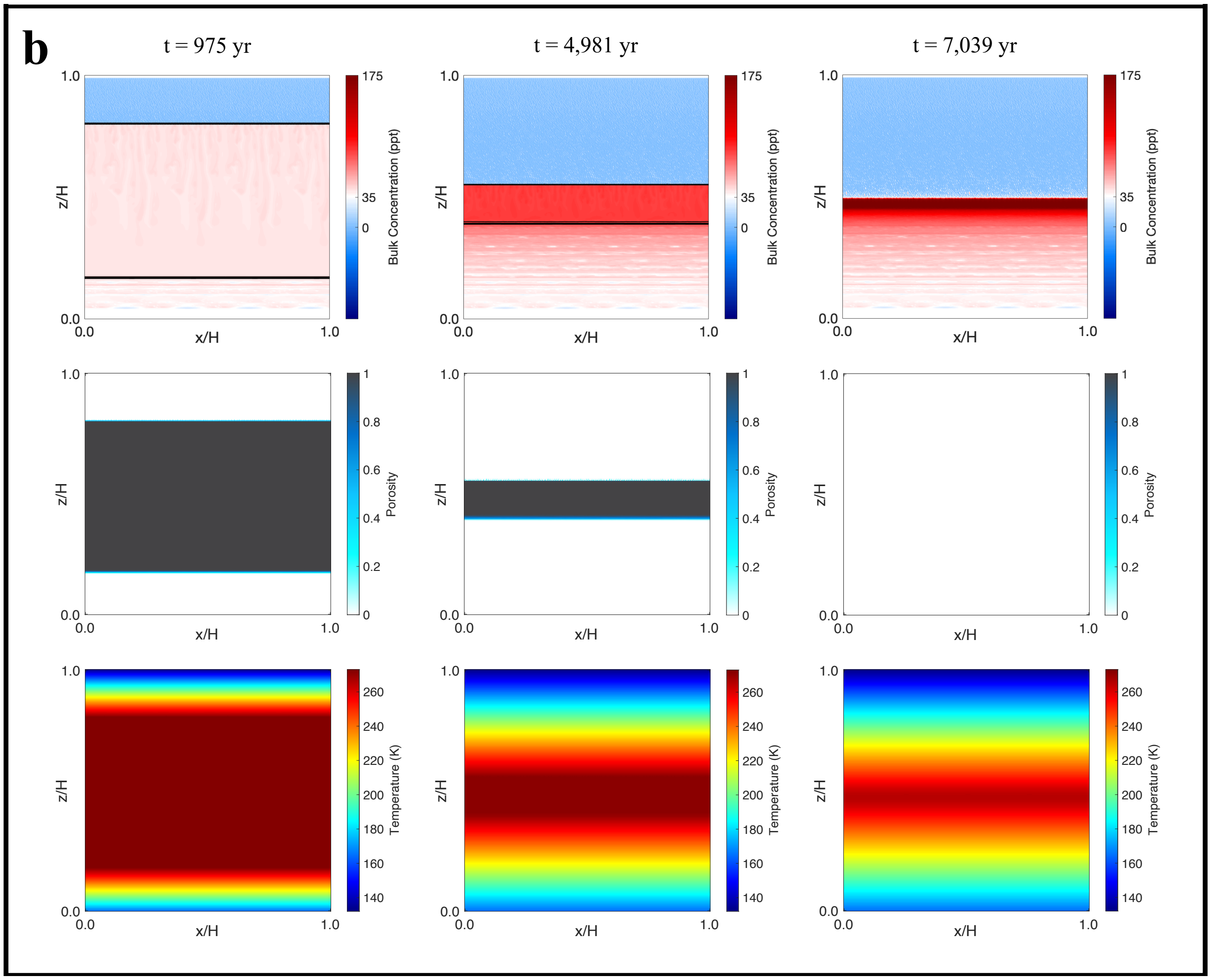


**Figure 3** – The thermal and physicochemical evolution of isolated saline sills in a brittle ice shell lithosphere. **a)** The spatiotemporal evolution of a 1 km thick 35 ppt NaCl sill subject to the undercooling boundary conditions presented in Figure 2. Rows: Top – bulk salinity (black contours demarcate porosities ranging from 0.15 to 0.95 in increments of 0.2); Middle – porosity; Bottom – temperature. Columns: temporal snapshots of the simulation. The third column represents the completely solidified sill (H = 1000 m). Note the thicker mushy layer at the sill floor compared to the sill roof, the dichotomy of salt retention at the sill floor and salt rejection at the sill roof, and the cryoconcentration of the residual brine as the simulation progresses. **b)** The spatiotemporal evolution of a 1km thick 35 ppt $MgSO_4$ sill subject to the undercooling boundary conditions presented in Figure 2. Rows and columns same as in panel (a) (H = 1000 m). Note the significantly thinner mushy layers compared to the NaCl simulation, a result of the reduced freezing point depression effects of $MgSO_4$. Detailed movies of the bulk salinity, porosity, and fluid dynamic evolution of the NaCl and $MgSO_4$ sills can be found in Supplementary Movies M1-M6.

Horizontally averaged vertical profiles of bulk salinity, porosity, and temperature can be seen in Figure 4. As the sills solidify salt is rejected from the roof of the chamber, salinating the residual brine. Conversely, all of the interstitial brine is retained in the basal multiphase solidification front, corroborating the work of *Chivers et al.* [2021], who predicted complete retention of salts in the solidifying floors of perched water lenses. This mechanism of complete retention is exemplified by the increasing bulk salinity values as the basal freezing front propagates upward from the initial sill floor, entraining higher concentrations of salt in the newly formed ice as the sill thins and increases in salinity. Upon complete solidification, both sills are left with a sheet of ice-salt mixture near the eutectic concentration of the respective ocean composition (230 ppt for NaCl and 175 ppt for $MgSO_4$). The thickness of this layer in the NaCl simulation is 15.6 m and that of the $MgSO_4$ simulation is 31.2 m (these thicknesses are for regions that possess bulk salinities within 1% of the eutectic concentration). *Chivers et al.* [2021] predicted that solidifying perched lenses of equivalent thickness (1 km) placed 1 km deep in a 5 km thick brittle ice lithosphere would produce *pure* salt lags ~1 m thick. Translating our eutectic layers into equivalent pure salt layers would produce thicknesses of 1.71-2.08 m.

Solidification times are represented by the rightmost columns of Figure 2a & 2b – 8,431 years for the NaCl sill and 7,039 years for the $MgSO_4$ sill. The longer solidification time for the NaCl sill is to be expected as NaCl depresses the freezing point of water more significantly than does $MgSO_4$. The multiphase solidification fronts at both the roof and floor of the NaCl sill are thicker than those of the $MgSO_4$ sill. This agrees with previous numerical and theoretical results [*Buffo et al.*, 2021a; *Buffo et al.*, *2020; Buffo et al.*, 2021b] that predict thinner multiphase regions for solutions whose eutectic temperatures are closer to the freezing point of pure water (i.e., solutes with less freezing point depression potential). In both the NaCl and $MgSO_4$ simulations, the multiphase layer at the sill floor is thicker than the multiphase layer at the sill roof, consistent with the lack of brine expulsion and multiphase layer trends in the roofs and floors of magmatic analogs [*Worster et al.*, 1990]. For an extended discussion of the multiphase evolution of sill roofs/floors and the influence of reservoir chemistry and thermal driving on their thicknesses and propagation rates see the Supplementary Material (Section S1 and Figures S1-S2).

The thermal profiles within the ice are very close to linear – suggesting conduction dominated heat transport in the surrounding ice – while the temperature of the residual brine is homogeneous – suggesting the fluid is well mixed (consistent with the assumption of *Chivers et al.* [2021]) – and decreases with time due to the salination of the brine and associated freezing point depression. Heterogeneities in bulk salinity in the lower portion of the solidified sills (e.g., horizontal variations in Figure 3a-b, oscillations in the bulk salinity profile of the $MgSO_4$ sill – Figure 4) are likely the result of downwelling saline plumes interacting with the basal solidification front (See Supplementary Movies M1, M3, M4, and M5). In reality, turbulence and convective mixing in the residual brine would likely dissipate these plumes before their impingement upon the sill floor (except perhaps near the end of the sill's solidification, when the residual brine reservoir is relatively thin) resulting in a more homogenous distribution of salt in the basally formed ice. The amplified plume stability is a result of implementing a finite permeability in the free fluid, which significantly optimizes computation time. The benefits and drawbacks of this approach are discussed at length in *Buffo et al.* [2021b], however given the general thermochemical homogeneity of the residual brine (Figure 4) we are confident that significant free fluid mixing is occurring and that our results are minimally affected by this optimization. The full spatiotemporal evolution of both sills can be found in Supplementary Movies M1-M6.

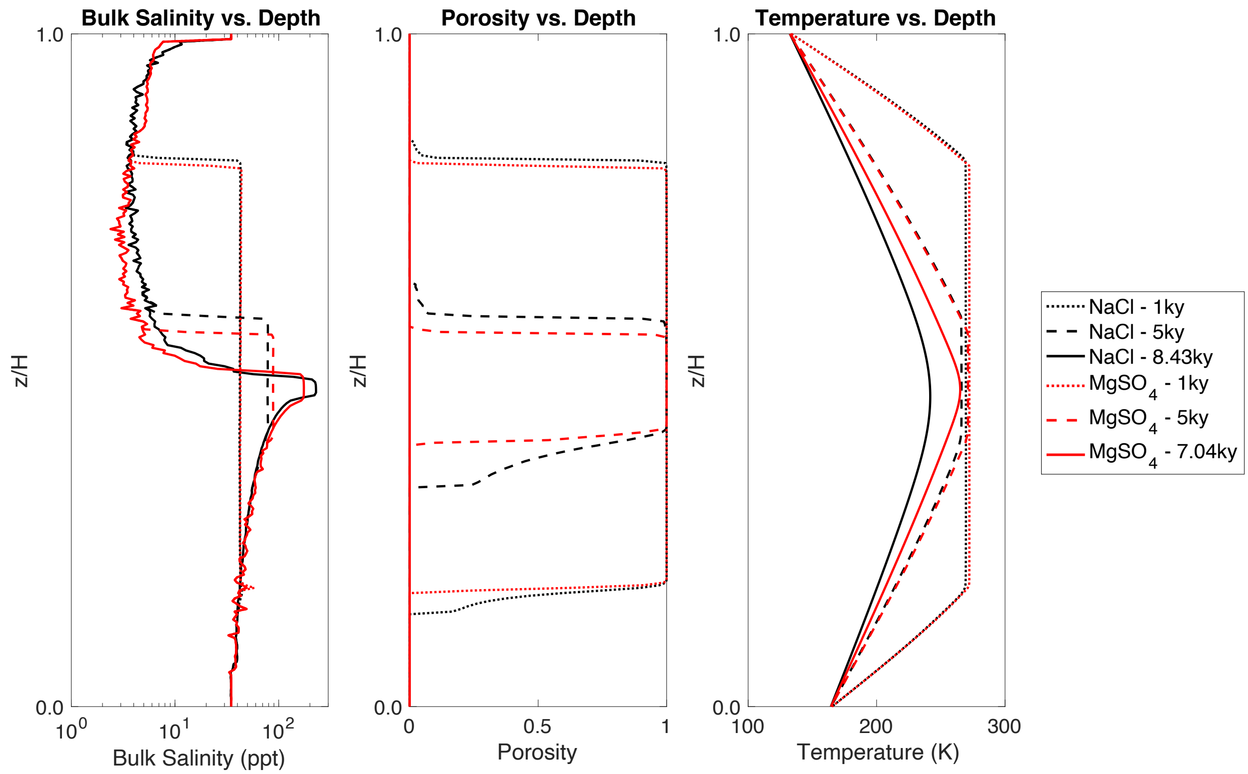


**Figure 4** – Vertical profiles of bulk salinity, porosity, and temperature during sill solidification (H = 1000 m). **Left)** Horizontally averaged vertical bulk salinity profiles of the NaCl and $MgSO_4$ sills depicted in the first rows of Figure 3a and 3b. Eutectic ice+hydrate mixtures can be seen as plateaus in the NaCl – 8.43ky and $MgSO_4$ – 7.04ky profiles at 230 ppt and 175 ppt, respectively. **Center)** Horizontally averaged vertical porosity profiles of the NaCl and $MgSO_4$ sills depicted in the second rows of Figure 3a and 3b. The vertical extents of the multiphase ice-brine interfacial layers can be seen thickening with time, consistent with contemporary theoretical and numerical predictions [*Buffo et al.*, 2021a; *Buffo et al.*, 2021b]. **Right)** Horizontally averaged vertical temperature profiles of the NaCl and $MgSO_4$ sills depicted in the third rows of Figure 3a and 3b. Temperatures within solid and mushy regions ($\phi < 1$) are representative of linear conductive thermal profiles, while the residual brines in the center of the sills ($\phi = 1$) are well mixed and are at their salinity dependent freezing points.

### 3.2 Fractures

A second type of hydrological feature that may be present in the ice shells of ocean worlds is fluid filled basal fractures. The same tidal heating that promotes the longevity of subsurface oceans on worlds like Europa and Enceladus also exerts cyclic stresses on the overlying ice shell. This combination of tensional, compressional, and rotational stresses has been suggested as a process capable of generating several of the fractural and other geological features seen across the surfaces of icy moons in the solar system (e.g., the tiger stripe fractures of Enceladus [*Nimmo*, 2020; *Rudolph and Manga*, 2009], ridges [*Dombard et al.*, 2013; *Head et al.*, 1997; *Hoppa et al.*, 1999; *Manga and Sinton*, 2004], dilational bands [*Howell and Pappalardo*, 2018; *Prockter et al.*, 2002], lenticulae [*Craft et al.*, 2016; *Fagents et al.*, 2000; *Manga and Michaut*, 2017], fractures [*Dombard et al.*, 2013; *Helfenstein and Parmentier*, 1983; *Nathan et al.*, 2019; *Rudolph and*

*Manga*, 2009; *Walker et al.*, 2014; *Walker et al.*, 2021], strike slip faults [*Hoppa et al.*, 2000; *Hoppa et al.*, 1999; *Kalousová et al.*, 2016; *Nimmo and Gaidos*, 2002], sill/lens/dike evolution [*Chivers et al.*, 2021; *Craft et al.*, 2016; *Manga and Michaut*, 2017; *Michaut and Manga*, 2014], and chaos formation on Europa [*Walker and Schmidt*, 2015], global scale fractures across less geologically modified icy worlds [Ganymede, Charon, Iapetus] [*Nathan et al.*, 2019]). Additionally, the solidification of the underlying ocean during initial ice shell formation or periodic/regional thickening will generate significant internal pressure, due to the density difference between ice and water, that could lead to fracture generation [*Berton et al.*, 2020; *Manga and Wang*, 2007]. If these fractures are connected to a fluid reservoir (either the underlying ocean or a perched water body within the shell) they are prone to infiltration by the fluid, upon which heat loss to the cold fracture walls should induce freezing of the injected brine. Given the significantly different geometry compared to top-down or bottom-up solidification and the indelible role interstitial fluid flow plays in resultant ice characteristics, this begs the question; what are the physicochemical characteristics of ocean/brine-derived ices that have grown along vertical fracture walls? To investigate the properties and evolution of ice grown in this geometric configuration we simulate the solidification of basal fractures filled with 35 ppt NaCl and $MgSO_4$ ocean water (a similar total salt content to Earth's ocean) at four different grid resolutions (7.8125E-3 m, 7.8125E-2 m, 7.8125E-1 m, and 7.8125 m).

**3.2.1 Solidification Evolution**

Temporal snapshots of the thermal and physicochemical evolution of NaCl ocean filled fractures simulated grid resolutions of 7.8125E-3 m and 7.8125 m (domain size: 1 meter by 2 m, and domain size: 500 meters by 2000 meters) can be seen in Figure 5a & 5b, respectively. As the fractures solidify inward salt is rejected from the forming ice and is transported downward into the underlying ocean via cold, dense, high salinity plumes that percolate through the sidewall mushy layer. These plumes are evident in both the high-resolution (Figure 5a) and low-resolution (Figure 5b) simulations, although they are much more prominent in the high-resolution simulation due to higher thermal gradients and more rapid ice formation (and thus brine rejection).

The most striking features produced during these simulations are the diagonally shaped brine channels that form along the fracture walls (See the porosity plots of Figure 5a). These high porosity, high salinity regions characterize the multiphase solidification interface and are responsible for transporting brine away from the propagating freezing front, akin to brine channels in sea ice [*Wells et al.*, 2019; *Worster and Rees Jones*, 2015]. The unique geometry of the problem (a horizontally propagating freezing front) results in a distinct 'V-shaped' pattern of high salinity regions as the channels solidify. This phenomenon is common in the solidification of multicomponent systems (e.g., metal alloys, aqueous solutions) and is referred to as A-segregation [*Bédard et al.*, 1992; *Campbell*, 2003; *Li et al.*, 2014]. The negative buoyancy of melt in ice-brine systems means the formation of macrosegregates occurs in the inverse direction – that is, A-segregation dynamics produce V-shaped rather than A-shaped channels. Given the widespread occurrence of analogous macrosegregation patterns in other systems, we believe that these features are realistic byproducts of a horizontal ice-brine solidification geometry and not the result of any numerical effects (e.g., numerical dispersion). While the lower resolution simulation (Figure 5b) does not exhibit channelization patterns, the continuum approach implemented by SOFTBALL guarantees that ice properties affected by brine drainage dynamics (e.g., bulk salinity) are still properly captured even when channels are not explicitly resolved (e.g., [*Buffo et al.*, 2021b]).

471 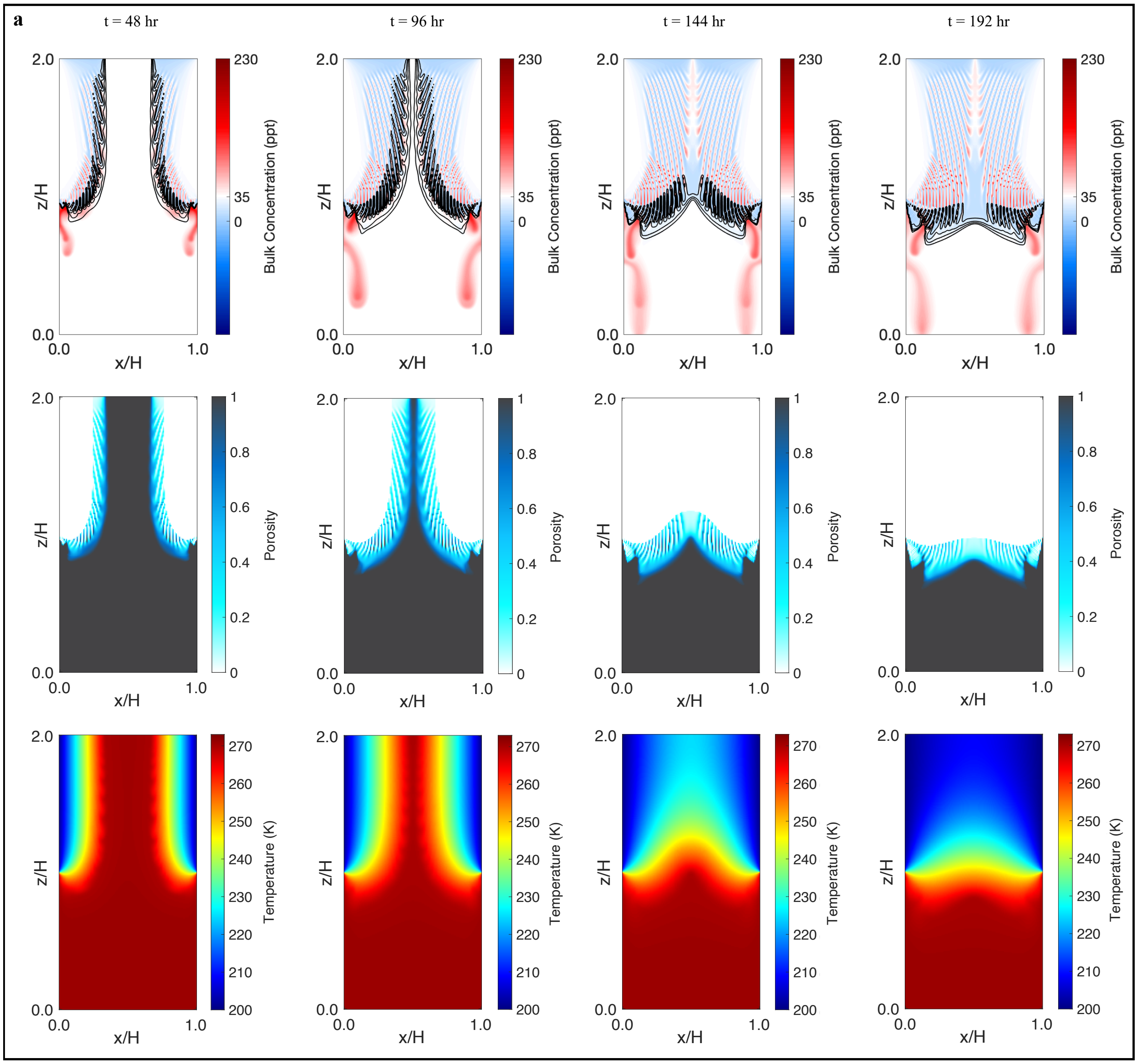

a
t = 48 hr
t = 96 hr
t = 144 hr
t = 192 hr
Bulk Concentration (ppt)
230
35
0
Porosity
1
0.8
0.6
0.4
0.2
0
Temperature (K)
270
260
250
240
230
220
210
200
z/H
x/H
2.0
0.0
1.0

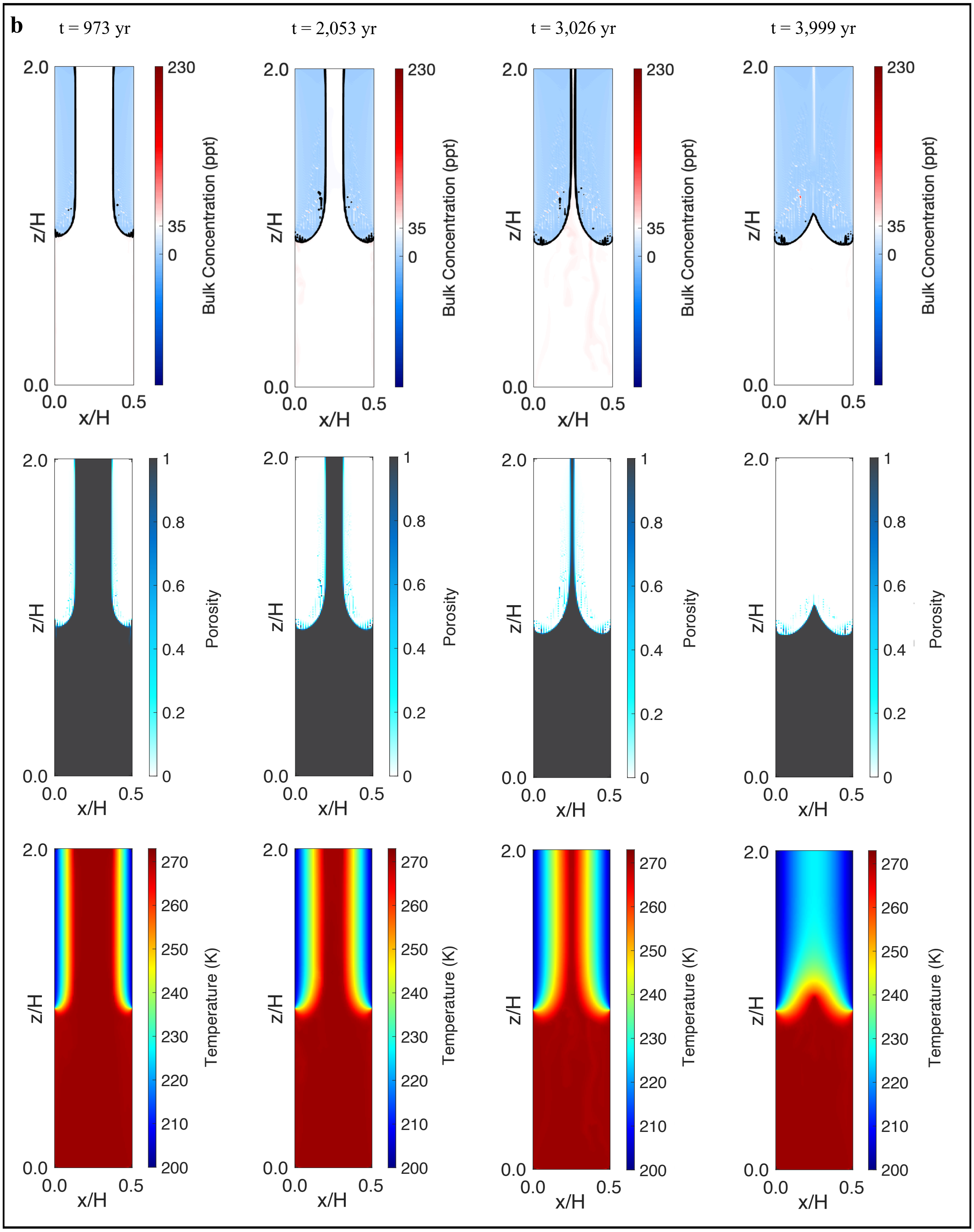


**Figure 5** – The thermal and physicochemical evolution of resolidifying basal fractures. **a)** A 1 m by 1 m 35 ppt NaCl ocean filled fracture (H = 1 m), highlighting the macrosegragation (formation of brine channels and ultimately inverted A-segregates) that occurs during the solidification of

brines. Note that the downwelling high salinity plumes do not flow out into the central portions of the fracture, but percolate downward through or at the boundary of the mushy layers that characterize the fracture walls (see Supplementary Movie M9 for exemplification of these dynamics via streamlines). Rows: Top – bulk salinity (black lines are porosity contours – 0.15 to 0.95 in increments of 0.2); Middle – porosity; Bottom – temperature. Columns: temporal snapshots of the simulation. **b)** A 500 m by 1000 m 35 ppt NaCl ocean filled fracture (H = 1000 m). While the coarser simulation does not explicitly resolve the macrosegregation textures seen in panel (a) the model's continuum approach guarantees that salt entrainment and associated chemical zonation patterns are still accurately captured (e.g., [*Buffo et al.*, 2021b]). Rows and columns same as in panel (a). Detailed movies of the bulk salinity, porosity, and fluid dynamic evolution of all the NaCl and $MgSO_4$ ocean filled fractures described in Table 2 can be found in Supplementary Movies M7-M33.

### 3.2.2 Resultant Bulk Salinity Profiles

As the fractures solidify the level of salt entrained in the newly formed ice is likely governed by the rate at which the fractures freeze (equivalently, the thermal gradient at the solidification interface). This logic is consistent with previous studies of ice formed in top-down solidification geometries under both Earth [*Griewank and Notz*, 2013; *Hunke et al.*, 2011] and planetary [*Buffo et al.*, *2020; Zolotov and Kargel*, 2009] conditions (e.g., sea ice, planetary ice shell formation) and the results of our sill solidification simulations (Section 3.1). In Figure 6, we plot the ultimate bulk salinity profiles of all fracture scenarios described in Table 2. In general, bulk salinities are highest near the distal edges of the fractures (where thermal gradients are the highest) and decrease towards the fracture centers, except for regions of high salinity that occupy the very centers of the solidified fractures where residual brine/salt has been trapped. The NaCl (Figure 6a-d) and $MgSO_4$ (Figure 6e-h) ocean filled fractures share many characteristics, including general bulk salinity trends, preserved brine channel structures, and more efficient salt rejection as thermal gradients decrease. The thinner mushy layers of the $MgSO_4$ systems are likely responsible for the enhanced salt entrainment at the distal edges of the fractures when compared to NaCl systems of the same scale (e.g., thicker regions of white near the outer portions of the fractures). The simulation subject to warmer sidewalls (Figure 6i – sidewalls at 260K) efficiently rejects salts from the ice due to the low thermal gradients at the solidification interface, however there are regions of residual liquid fraction in the ice ('freckles' seen in Figure 6i). This is because 260K is above the eutectic point of the NaCl system, meaning that regions with even small amplifications in bulk salinity (e.g., relict brine channels) can remain in a liquid state in the relatively temperate ice.

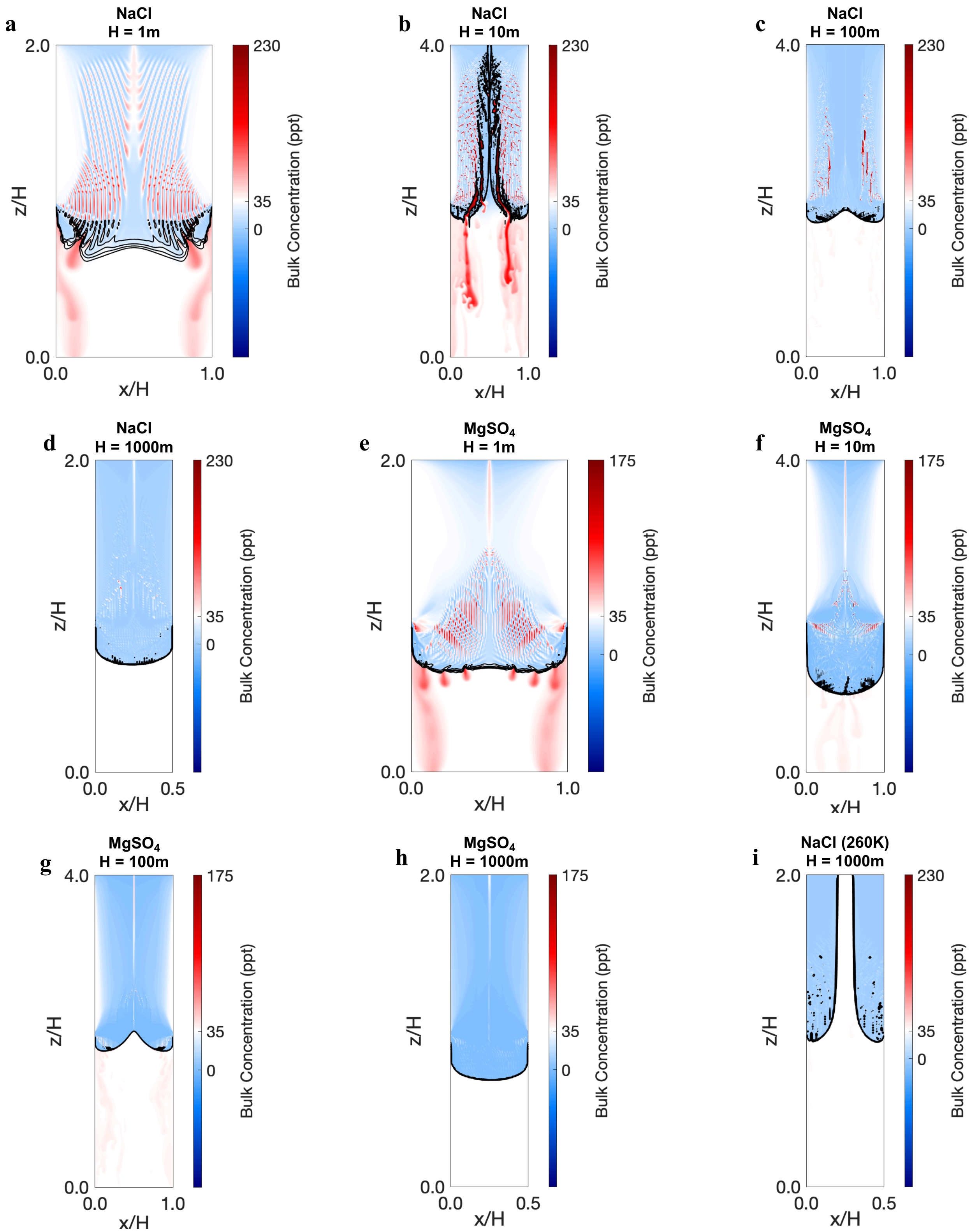


**Figure 6** – Bulk salinity profiles of solidified fractures. These plots show the final frame of the nine fracture simulations described in Table 2. **a)** 1 m by 1 m 35 ppt NaCl ocean filled fracture. **b)** 10 m by 20 m 35 ppt NaCl ocean filled fracture. **c)** 100 m by 200 m 35 ppt NaCl ocean filled

fracture. **d)** 500 m by 1000 m 35 ppt NaCl ocean filled fracture. **e)** 1 m by 1 m 35 ppt $MgSO_4$ ocean filled fracture. **f)** 10 m by 20 m 35 ppt $MgSO_4$ ocean filled fracture. **g)** 100 m by 200 m 35 ppt $MgSO_4$ ocean filled fracture. **h)** 500 m by 1000 m 35 ppt $MgSO_4$ ocean filled fracture. **i)** 500 m by 1000 m 35 ppt NaCl ocean filled fracture with 260K sidewall undercooling. Simulations where the sidewalls did not freeze together by the end of the simulation, panel (b) and (i), were due to instabilities that effected the convergence of the model (in the case of panel (b)) and long run times due to lower sidewall undercooling (in the case of panel (i)). Detailed movies of all fracture solidification simulations can be found in Supplementary Movies M7-M33.

To quantitatively investigate the impacts of a horizontal freezing geometry on the level and spatial heterogeneity of salt entrainment in basal fractures, we sample two distinct types of horizontal bulk salinity profiles. The first consists of horizontal profiles along the topmost domain elements of all fracture simulations. We select this profile to isolate the effects of horizontal solidification geometry on salt entrainment rates from the impacts of heterogeneous fluid composition and dynamics along the vertical length of the fracture. That is, the topmost layer of the domain is uncontaminated by any downwelling brine from higher in the ice (which we will show significantly impacts salt entrainment) and thus represents a 'control' signal to investigate the effects of horizontal solidification on the amount of salt entrained in the ice. The most useful comparison to be made (both across simulations and with previous studies of salt entrainment – e.g. [*Buffo et al.*, 2021b]) is the relationship between bulk salinity of the newly formed ice and the interfacial thermal gradient at the time of solidification, as this is more agnostic than comparisons with depth or distance, which depend on the specific environmental parameters of the system. This comparison is relatively straightforward as thermal gradients within the ice are well represented by linear conductive profiles (e.g., Figure 4 and Figure 5). In Figure 7 we plot the relationship between ice bulk salinity and interfacial thermal gradient for the topmost cells of all fracture simulations shown in Figure 6.

To contextualize our simulated fracture bulk salinities with those predicted to occur in top-down solidification geometries and determine if bulk salinity-thermal gradient relationships are consistent across freezing geometries we compare our results to those of *Buffo et al.* [2021b], who leveraged the work of *Buffo et al.* [*2020*] to analytically derive a functional relationship between bulk salinity and interfacial thermal gradient in top-down solidification scenarios:

$$C\left(\frac{\partial T}{\partial x}\right) = a + \left(\frac{-b\left(\frac{\partial T}{\partial x} - c\right)}{-d - f\frac{\partial T}{\partial x}}\right)\left(1 + h\exp\left(\frac{-j}{\partial T/\partial x}\right)\right) \qquad (1)$$

where $C$ is bulk salinity in [ppt], $T$ is temperature in [K], $x$ is distance in [m] and $a, b, c, d, f, g, h$ and $j$ are constant coefficients that account for variations in the composition and concentration of the ocean/brine being frozen and the dynamics of brine convection in the mushy layer [*Buffo et al., 2020; Buffo et al.*, 2021b]. In Figure 7 we plot the relationship between bulk salinity and interfacial thermal gradient derived by *Buffo et al.* [2021b] for the top-down solidification of a planetary ice shell from a 35 ppt saline ocean (liquidus slope ($m$) of 0.048 K $ppt^{-1}$, and solutal contraction coefficient ($\beta$) of 5.836E-4 kg $ppt^{-1}$):

$$C\left(\frac{\partial T}{\partial x}\right) = 7.864 + \left(\frac{-2576\left(\frac{\partial T}{\partial x} - 5.148\right)}{-2067 - 869.2\frac{\partial T}{\partial x}}\right)\left(1 + 10.93\exp\left(\frac{-27.2}{\partial T/\partial x}\right)\right) \tag{2}$$

To determine if a comparable functional relationship can describe our simulated refrozen fracture bulk salinities, thus capturing the underlying multiphase physics of the analytical top-down solution while accounting for the additional effects of a horizontal freezing geometry, we seek a bulk salinity-thermal gradient relationship that varies minimally from that of the top-down solidification configuration (Equation 2). Accordingly, we fit our simulation results to a simple log-linear translation of the bulk salinity-thermal gradient relationship described by Equation 2:

$$C'\left(\frac{\partial T}{\partial x}\right) = C\left(\exp(a)\frac{\partial T}{\partial x}\right) - b \tag{3}$$

where $a$ and $b$ are constant coefficients that account for the geometric effects of horizontal solidification. In Figure 7 we plot a Levenberg-Marquardt algorithm best fit of Equation 3 to the fracture bulk salinities simulated during this work:

$$C'\left(\frac{\partial T}{\partial x}\right) = C\left(\exp(4.05)\frac{\partial T}{\partial x}\right) - 1.153 \tag{4}$$

The bulk salinities produced by the horizontal solidification of fractures are less than those produced during top-down solidification scenarios under comparable thermal forcing. This is likely caused by more efficient brine drainage in the multiphase fracture walls than in horizontal mushy layers beneath vertically growing ice, which must overcome a Rayleigh-Taylor instability for convective brine drainage to occur [*Griewank and Notz*, 2013; *Notz and Worster*, 2009]. We discuss the geophysical implications of this variance in salt entrainment in Section 4.2. Equation 4 captures the relationship between interfacial thermal gradients and resultant ice bulk salinity for both the NaCl and $MgSO_4$ oceans, which can likely also be attributed to the system not needing to overcome a critical Rayleigh number for brine drainage to occur in the mushy layers of the fracture walls. This, again, contrasts with horizontal mushy layers beneath vertically growing ice, where variable ocean composition impacts mushy layer thickness, onset and behavior of Rayleigh-Taylor convection within the mushy layer, and ultimately the rate of salt entrainment in the ice (e.g., differences in the bulk salinity profiles of our simulated sills (Figure 4) and *Buffo et al.* [*2020*]).

As thermal gradients decrease so does salt entrainment, less the amplifications at the centers of the fractures caused by interactions with the opposite fracture wall. In all of the simulations there are three distinct regimes: 1) at high thermal gradients, prior to the growth of a mushy layer that is greater than one discretization cell thick, there are amplified levels of salt entrainment due to a lack of resolution (this is supported by the fact that $MgSO_4$ simulations, with their thinner mushy layers, spend a longer time in this regime); 2) once a mushy layer greater than one cell thick is established and the fracture is freezing inward, but hasn't begun interacting with the other fracture wall, convective overturn (gravity drainage driven desalination) in the mushy layer occurs and governs the resultant salt entrainment in the forming ice; and 3) at the end of solidification an amplified level of salt entrainment at the center of the fracture occurs due to reduced fluid flow in the narrowing fracture and any residual brine is trapped. One notable exception is the simulation of the 100 m by 200 m 35 ppt NaCl ocean filled fracture, which generated freshwater plumes during rapid brine drainage events that buoyantly rose and filled the fracture center, resulting in a significantly freshened bulk salinity profile within the central region of the fracture and a dearth of the typical Regime 3 spike (See Figure 4c and Supplementary Movies M13-M15).

Regime 1 is not physically realistic and is the result of not resolving the mushy layer (i.e., finite discretization leads to a one-dimension mushy layer that does not support vorticity to drive/resolve convection). Similar anomalous amplifications in ice bulk salinity were observed by *Buffo et al.* [2021b] when simulating the top down solidification of planetary ice shells (their Figure 3d-f). The final phase of fracture solidification – when the two fracture walls begin to interact and ultimately freeze together – is a classic example of a non-isolated system. That is, the resulting spatial heterogeneity is due to dynamic interactions between the fracture walls and not a result of horizontal freezing alone. In Figure 7b we plot only the second regime, excluding bulk salinities generated by thin (1 cell thick) mushy layers as well as the central portions of the fractures with amplified salinities. With the influence of horizontal solidification isolated (Figure 7b), the translated relationship of *Buffo et al.* [2021b] (Equation 4, dashed line of Figure 7) fits the simulated bulk salinities exceptionally well.

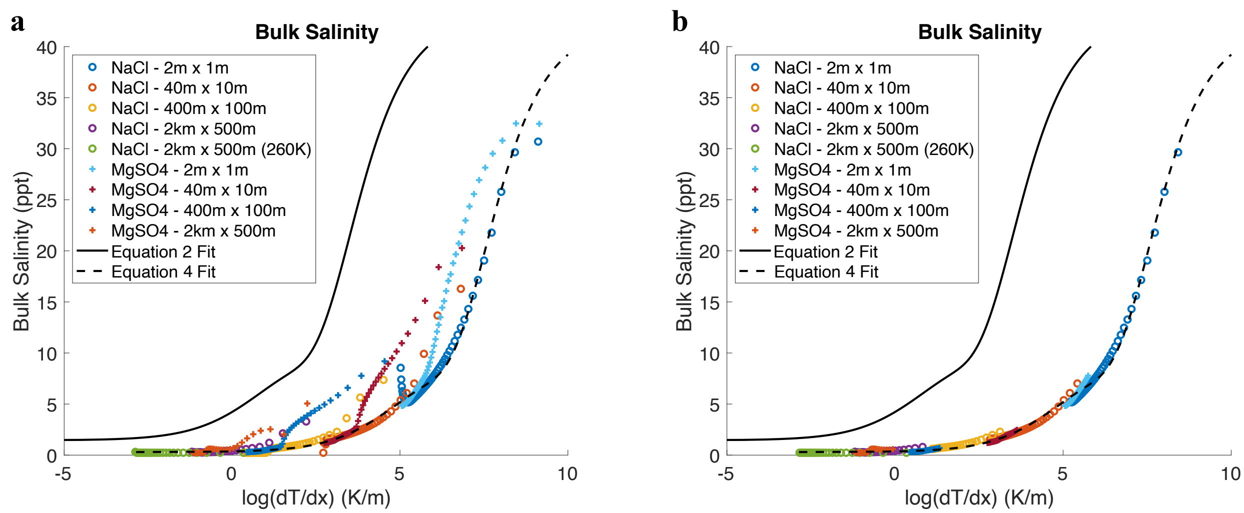


**Figure 7** – The impact of ice-ocean/brine interfacial thermal gradient on impurity entrainment in solidifying basal fractures. **a)** The relationship between the interfacial thermal gradient at the time of ice formation and the amount of salt retained in the ice. This plot includes all the raw data extracted from the top discretized row of the domain for all the fracture simulations outlined in Table 1 except the central amplifications/depletions (Regime 3 outlined in the text). The solid black line is the relationship between salt entrainment and thermal gradient for top-down solidification geometries derived by *Buffo et al.* [2021b] (Equation 2). The dashed black line is the best fit log-linear translation of this line to the current data (Equation 4). **b)** This plot contains the same data and fit lines as panel (a) but data points that were acquired when the interfacial mushy layer was less than one discretization cell thick (Regime 1) have been removed.

In addition to horizontal trends in bulk salinity driven by variable thermal gradients, there are vertical variations in the bulk salinity profiles of the solidified fractures. Figure 8a-c show the two-dimensional bulk salinity (a), temperature (b), and porosity (c) profiles of a 10 m by 20 m solidified basal fracture initially filled with a 35 ppt $MgSO_4$ ocean. Figure 8d-f highlight five distinct vertical regions within the fracture where we investigate the mean horizontal bulk salinity profile (d), shows the fine scale vertical variations in horizontal bulk salinity of the upper region (e), and plots the mean horizontal bulk salinity profiles of the five regions (f). In the plots of horizontal bulk salinity (Figure 8e & 8f), the bulk salinity of the solidified fracture increases with depth; that is, ice formed in deeper portions of the fracture retains more salt than ice subject to the same thermal gradients (i.e., ice at the same distance from the domain's distal edges) in higher portions of the fracture. We discuss physical mechanisms that could cause this vertical trend to occur in Section 4.2. This amplification of bulk salinity with depth occurs across all ocean chemistries and simulation resolutions. In Figure 8g-h we plot the bulk salinity versus thermal gradient for various depths within 35 ppt NaCl ocean filled fractures (Figure 8g is raw data while Figure 8h removes the data from Regime 1 and 3 discussed above). We include an inset in Figure 8h of the same data plotted in log-log space to highlight an interesting near-linear relationship between log $(\partial T/\partial x)$ and log $(C)$. Again, it is evident that lower portions of the fracture will retain more salt than higher regions subject to the same thermal forcing. The implications of this vertically heterogeneous salt retention on icy world geophysics and ocean-surface transport are discussed in depth in Section 4.

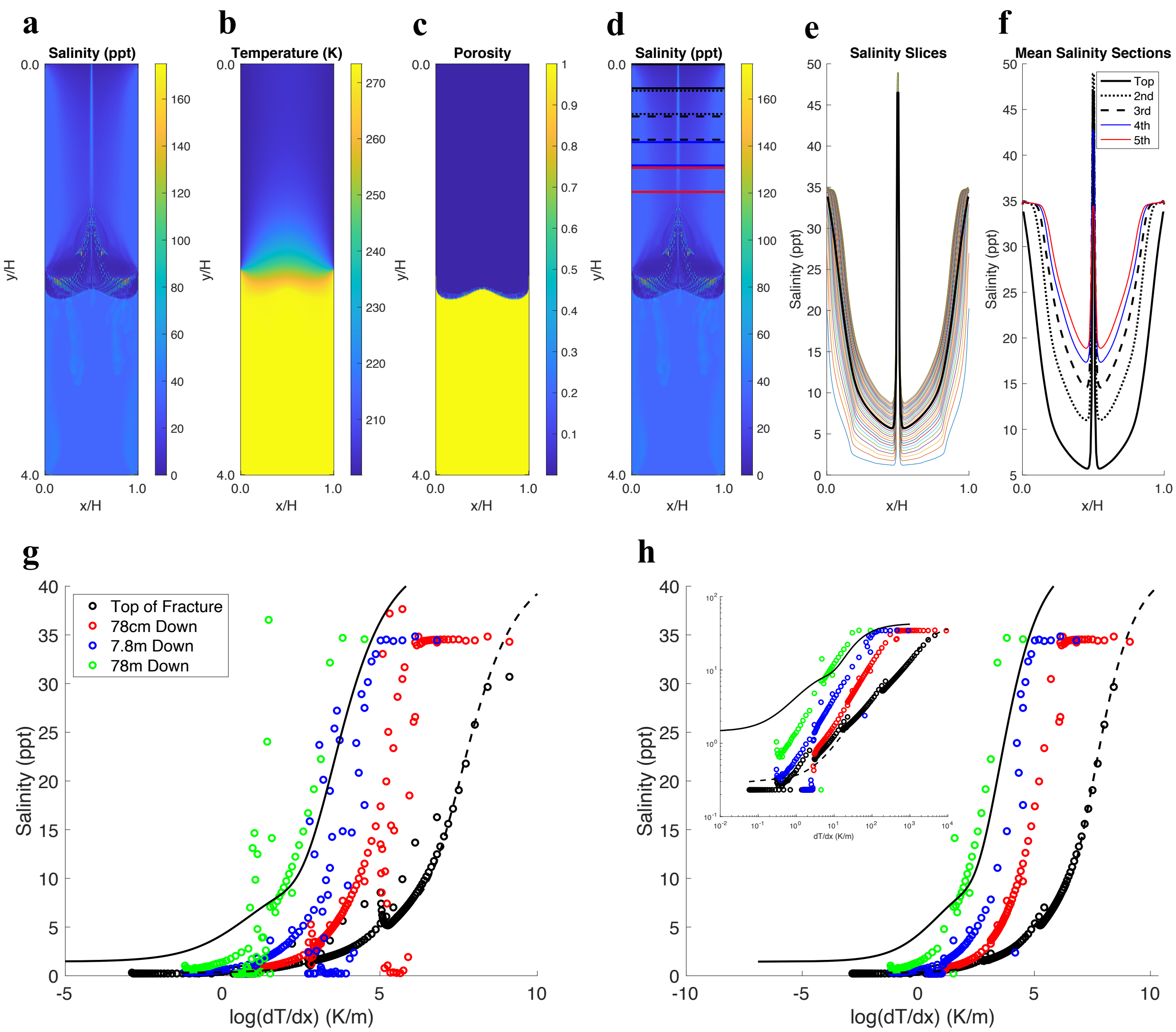

**Figure 8** – Heterogeneous spatial distributions of salt retention within solidified basal fractures. **a)** The bulk salinity distribution in a 10 m by 20 m (H = 10 m) solidified basal fracture that was initially filled with a 35 ppt $MgSO_4$ ocean (200K sidewall undercooling). **b)** The temperature profile of the basal fracture depicted in panel (a). **c)** The porosity profile of the basal fracture depicted in panel (a). **d)** This plot is identical to panel (a) but highlights the five discrete regions where we explore vertical trends in salt retention (See panels (e) and (f)). **e)** Horizontal bulk salinity profiles of the top 32 discretized rows of the simulated domain (space between the top two solid black lines of panel (d)). Colored lines – the top row of the simulation domain is the blue line with the lowest bulk salinity and each consecutive row has a higher bulk salinity. The black solid line is the vertically averaged horizontal bulk salinity profile of the top 32 rows of the simulation domain. **f)** Vertically averaged horizontal bulk salinity profiles of the regions depicted in panel (d). Note the increasing bulk salinity of the ice with depth. **g)** The relationship between interfacial thermal gradient and salt entrainment for different depths within solidified basal fractures. This plot includes data from all NaCl fracture simulations listed in Table 2. The solid and dashed black lines are the fit lines described by Equations 2 and 4, respectively. **h)** This plot contains the same data as panel (g), but, like Figure 6b, data points generated in regions where the interfacial mushy layer was only one discretization cell thick (Regime 1) or interacting with the opposite fracture wall (Regime 3) have been removed. Inset – The same plot in log-log space.

## 4. Discussion

### 4.1 Sills

The bidirectional solidification of sills in Section 3.1 highlighted the role of gravitational instability-driven convection in the interfacial mushy layer of forming ice as the principal mechanism of ice desalination in ice-ocean/brine systems. This is epitomized by the complete retention of salt in ice formed via bottom-up solidification – i.e., the floors of the sills – contrasted with the efficient expulsion of brine from sill ceilings forming via top-down solidification. This process of salt retention is facilitated by the gravitational *stability* of the interstitial brine in the basal mushy layer, precluding convective overturn and desalination. Furthermore, a large Lewis number (>>1) for all systems considered here means there is no appreciable diffusion of salt out of the interfacial mushy layers as the ice growth rate due to thermal diffusion will outpace molecular diffusion (this rationale was previously highlighted by *Chivers et al.* [2021]). The ultimate chemical signature of a solidified intruded sill will be characterized by three zones: 1) a relatively fresh upper region that has formed via top-down solidification, where decreasing salt retention occurs with decreasing thermal gradient (increasing depth) and increased salt retention occurs near the central portion of the sill as the residual fluid concentrates; 2) a high salinity lower region formed via bottom-up solidification, where salt retention will reflect the sill chemistry at the time of ice formation; and 3) a central portion of the sill containing a eutectic mixture of ice and salt hydrates resulting from the residual fluid saturating (Figure 3 & 4).

The properties and dynamics highlighted here (e.g., perfect salt retention in the sill floor, trends in the resultant chemical profiles of solidified isolated water bodies, a high salinity eutectic layer at the sill center) are in excellent agreement with the predictions of *Chivers et al.* [2021] who simulated the two-dimensional thermochemical evolution of perched saline lenses in Europa's ice shell using the salt entrainment parameterizations of [*Buffo et al., 2020*] (See Figure 7 & 8 of *Chivers et al.* [2021] in comparison to our Figure 3 & 4). Our predictions for the freeze out times of 1 km thick sills intruded 1 km deep in a 5 km thick brittle Europan lithosphere (8,431 years for 35 ppt NaCl filled sills and 7,039 years for 35 ppt $MgSO_4$ filled sills) are consistent with *Chivers* *et al.* [2021]'s simulations of 1 km thick lenses intruded 1 km below the surface in a 5 km thick conductive lithosphere (8,400-15,400 years depending on whether they are located at the pole or equator). The reduced solidification times in our study can be accounted for by the fact that *Chivers et al.* [2021] simulated a larger domain and included heat loss to the surrounding ice, whereas our simulations did not account for this insulative warming (boundaries of the domain were held at constant low temperature) and thus will overpredict the rate of heat loss from the intruded sill. Additionally, the quantity of residual salt associated with the saturated liquid at the final stage of solidification is consistent across both investigations (~1 m pure salt for *Chivers et al.* [2021] and 1.71-2.08 m of pure salt in the current study – calculated from our simulated eutectic ice-salt layer thicknesses of 15.6-31.2 m). The quantitative and qualitative consistencies between *Chivers et al.* [2021] and our present work gives credence to both investigations, suggesting the parameterizations implemented by *Chivers et al.* [2021] are representative of the multidimensional reactive transport physics explicitly captured by SOFTBALL, and demonstrating that SOFTBALL accurately simulates the complex thermal and physicochemical evolution of ice-ocean/brine systems, including our concomitant investigation of fracture solidification.

There are several important geophysical and astrobiological implications related to the chemically heterogeneous solidification of perched water features within planetary ice shells. Fundamentally, chemical heterogeneities in planetary ice shells will likely be associated with collocated gradients in other material properties (e.g., strength, rheology, melting point, density, reactivity) [*Durham et al.*, 2005; *Han and Showman*, 2005; *McCarthy et al.*, 2011; *Pappalardo and Barr*, 2004; *Toner et al.*, 2014]. Given the variety of ice shell dynamics hypothesized to be driven or amplified by heterogeneities within the ice (e.g., thermocompositional solid state convection, subduction/subsumption, eutectic melting, ocean-surface interaction, brittle lid dynamics, multiphase reactive transport processes), understanding cryohydrologic processes that can produce such heterogeneities is imperative in expanding our understanding of ice-ocean world systems [*Buffo et al.*, *2020; Buffo et al.*, 2021b; *Vance et al.*, 2020]. The ability to predict the chemical evolution of hydrologic features within the ice shells of ocean worlds is also integral in assessing the habitability and biosignature preservation capabilities of planetary ices [*Arnold et al.*, 2019; *Schmidt*, 2020; *Schmidt and Buffo*, 2017; *Vance et al.*, 2016; *Vance et al.*, 2018]. Beyond identifying the location and longevity of aqueous environments within planetary ice shells that may act as habitable niches, assessing the evolution of biologically relevant water properties such as salinity, water activity, and chao-/kosmotropicity that impact life and its function will be fundamental in quantifying the spatiotemporal habitability of ocean worlds [*Buffo et al.*, 2022; *Cosciotti et al.*, 2019; *Fox-Powell and Cockell*, 2018; *Hallsworth et al.*, 2007; *Pontefract et al.*, 2019]. Moreover, if the evolving reservoir chemistry of perched water bodies is recorded in the compositional stratigraphy of their resolidified floors, they could provide an observable means of reconstructing the geochemical evolution and habitability of liquids within the shell long after they have frozen solid.

### 4.2 Fractures

The two-dimensional reactive transport simulations of horizontally freezing ice-ocean/brine interfaces conducted here are, to our knowledge, the first of their kind. While other works have simulated the multidimensional solidification of water bodies (e.g., [*Buffo et al.*, *2020; Chivers et al.*, 2021; *Hesse and Castillo-Rogez*, 2019]) these studies implement parameterizations for material entrainment rather than explicitly simulating the multiphase dynamics of the interfacial ice-brine mushy zone. With the goal of investigating the dynamics of hydrological feature sidewall freezing (e.g., vertical fractures, dikes, the sidewalls of liquid reservoirs such as lenses), our results exhibit several novel characteristics and behaviors that suggest the geometry of solidification fronts will have significant impacts on the ice's structural, thermochemical, and material properties. These properties have direct implications for the geochemistry and geophysics of planetary ices and the dynamics associated with nonplanar and nonvertical solidification fronts may provide physical mechanisms for introducing amplified and heterogeneous material loads into planetary ice shells.

The most fundamental observation in our simulations of horizontal solidification is the presence of diagonally oriented brine channels that populate the interfacial mushy layer during growth and ultimately solidify as high salinity macrosegregates (e.g., the high-resolution simulations of Figure 5a). The occurrence of brine channels is to be expected as the gravitational instability of brine in the growing mushy layer leads to the convective downwelling of brine away from the propagating interface (akin to the physical process of gravity drainage desalination observed in the planar mushy layer interfaces of sea ice [*Griewank and Notz*, 2013; *Notz and Worster*, 2009] and the ceilings of the sills simulated in Section 3.1). Here we suggest that the diagonal orientation of the channels is also to be expected based on analogy to the formation of A-segregates during the solidification of multicomponent metal alloys.

During the cooling and solidification of multicomponent metal alloy castings for industrial or engineering use there will always occur some amount of macrosegregation – localized ionic or molecular enrichments that depart from a uniform distribution of chemical elements in the alloy brought about by the multiphase reactive transport dynamics associated with solution solidification [*Campbell*, 2003]. As multicomponent alloys cool (e.g., ingot castings) they begin to fractionally crystallize, solidifying in a columnar fashion from the casting walls and rejecting solutes that cannot be incorporated into the growing crystal lattice (e.g., carbon, sulfur, and phosphorous in the case of steel) into the interdendritic spaces of the forming mushy layer (Figure 9b) [*Campbell*, 2003]. In metal alloy systems the solute-rich melt is less dense than the background liquid, driving the buoyant ascension of plumes through the interfacial mushy zone. The depressed melting point of the solute rich melt leads to the dissolution of channels/chimneys upon its ascension and the ultimate formation of A-channel segregates once the ingot completely solidifies (Figure 9b & 9c). The physics governing the formation of A-segregates in metal alloy systems is identical, but inverted, to those driving the V-shaped amplifications of salt in the frozen fracture simulations. As salt is rejected from forming ice crystals it produces a negatively buoyant brine in the pore space of the interfacial mushy layer. Gravity drainage drives downward convection of the brine, where it dissolves paths through existing dendritic ice structures and leads to the formation of high salinity brine channels (Figure 9b). Ultimately, these channels are frozen into the ice of the solidified fracture, introducing heterogeneities in ice structure and chemistry compared to the surrounding 'country' ice in which the fracture was emplaced (Figure 9c). Concomitant heterogeneities in the ice's material properties (e.g., ice strength, rheology, melting point) could make fractures susceptible to reactivation long after they have solidified (e.g., via tidal stresses, tidal heating, or eutectic melting) and constitutes a likely widespread geological process capable of introducing variable composition, structure, and material properties into planetary ice shells.

While we do not explicitly model free floating crystal formation in our ice-brine system simulations, a common process observed in both magmatic and metallurgic analog systems (e.g., Figure 9b), we do observe freshwater melt plumes pooling at the fracture tips during some model runs (e.g., Supplementary Movie M13). Such buoyantly rising masses of freshwater have the potential to form frazil/platelet ice crystals via the ice pump mechanism (depressurization crystallization) – potentially infilling fractures with an inverted snowfall of ice crystals (akin to marine/frazil ice accretion on Earth [*Craven et al.*, 2009; *Fricker et al.*, 2001; *Galton-Fenzi et al.*, 2012; *Holland et al.*, 2009; *Khazendar and Jenkins*, 2003; *Khazendar et al.*, 2009; *Lawrence et al.*, 2020; *McGuinness et al.*, 2009; *Smedsrud and Jenkins*, 2004]) and leading to an analogous region of segregation (in this case exceptionally fresh ice [*Wolfenbarger et al.*, 2018; *Wolfenbarger et al.*, 2019]) at the fracture tip. SOFTBALL does not currently account for the pressure dependent freezing point depression of the ocean.

On a larger scale there are two important compositional trends that occur during fracture freezing, one horizontal and one vertical. As the fractures freeze inward and the thermal gradients driving continued solidification decrease the rate of salt entrainment decreases. This result is consistent with previous studies of top-down solidification (e.g., [*Buffo et al., 2020; Buffo et al.*, 2021b; *Griewank and Notz*, 2013]) as well as chemical zonation patterns observed in solidifying mafic dikes, metal alloys, and aqueous salt solutions [*Chistyakova and Latypov*, 2009; *Chistyakova and Latypov*, 2010; *Hebditch and Hunt*, 1974; *Huppert*, 1990; *Leitch*, 1985] (Figure 9a and 9d) – terrestrial analogs of these fracture systems. Furthermore, the functional relationships between thermal gradient and material entrainment rate are consistent with previous investigations [*Buffo et al.*, 2021b], only requiring simple translations in logarithmic-linear space to account for the geometric effects on resultant ice salinity (Section 3.2.2) – suggesting the physics of multiphase reactive transport still dominate the evolution of the system. In isolating the effects of horizontal solidification on salt retention (that is, focusing on the uppermost portion of the fracture that is unmodified by infalling brine) we have shown that brine is more readily expelled from the mushy layer and results in lower salt retention than would be expected for ice formed via top-down solidification subject to the same thermal gradient. This is due to the unconditional density instability that initiates downward convection of the brine in the sidewall mushy layer (a fundamental restriction that governs the initiation and continuation of convective overturn in mushy layers grown by top-down solidification [*Griewank and Notz*, 2013; *Notz and Worster*, 2009]). The horizontal chemical gradation within the solidified fractures will result in associated spatial variations in ice material properties that could result in the strengthening or weakening of these regions depending on the impurity load and composition [*Assur*, 1958; *Durham et al.*, 2005; *McCarthy et al.*, 2011] – making them either susceptible or resilient to reactivation via both mechanical and thermal processes (e.g., tidal stress, melting).

In addition to horizontal chemical gradients within the refrozen fractures there exist distinct vertical trends in salt entrainment. Highlighted in Section 3.2.2, lower portions of the resolidified fractures retain higher levels of salt than upper portions of the fractures that have been subject to the same thermal gradient (e.g., Figure 8g-h). We believe this is caused by the downward percolation of high salinity brine through the mushy layer from the upper reaches of the fracture as the lower walls continue to freeze inward. That is, unlike the upper portions of the fracture's mushy layers, which are refreshed by upwelling ocean water present in the central liquid region of the fracture (see the velocity vectors and streamlines of Supplementary Movies M9, M12, M15, M18, M21, M24, M27, and M30) resulting in relatively fresh ice, the lower portions of the mushy layers are flushed with brine that is continually concentrating (due to continued freezing - cryoconcentration) as it percolates downward through the multiphase walls of the fracture, producing increasingly saltier ice. These lower reaches of the fracture receive minimal to no freshening via circulation of upwelling ocean water through the interior of the fracture, evidenced by the lack of streamlines entering the sidewall mushy layers in Supplementary Movies M9, M12, M15, M18, M21, M24, M27, and M30. This is a novel result for cryohydrologic systems that, to our knowledge, has not been investigated in naturally occurring analog systems on Earth (e.g., measurement of chemical zonation in sea ice leads or congelation ice growth in ice shelf basal fractures), however similar zonation patterns *have* been observed in laterally solidifying aqueous solutions in the laboratory [*Leitch*, 1987]. While lateral chemical zonation in magmatic dikes has been observed (Figure 9a), variable zonation in the vertical direction (i.e., the amplification of solute retention with depth as observed in our ice-brine simulations) has not been measured or reported in the literature. It is important to note that this does not preclude such vertical zonation in magmatic systems and searching for examples of such vertical zonation could potentially be a fruitful analog investigation.

The analog system that exhibits the strongest similarity to our ice-brine systems (and is the most well studied) is the solidification of metal alloys. In addition to the presence of A-segregates, whose governing physics mimic and explain the formation of the V-shaped salinity amplifications observed in our resolidified basal fractures (Figure 9b-c), and the occurrence of lateral variations in solute retention driven by variable thermal gradients, metal alloy castings exhibit vertical variations in solute distribution driven by the ongoing concentration of melt as it buoyantly percolates through the actively propagating mushy layer (e.g., Figure 9b-c) [*Hebditch and Hunt*, 1974; *Huppert*, 1990]. In the case of confined metal alloy castings this results in the formation of A-segregates as channels are dissolved and ultimately crystallize in the mushy dendritic zone as well as larger regions of positive and negative segregation driven by solute and crystal buoyancy, respectively (Figure 9b-d) [*Campbell*, 2003; *Hebditch and Hunt*, 1974; *Huppert*, 1990]. These features have been empirically observed in the laboratory and successfully simulated using two-dimensional multiphase reactive transport models akin to the one implemented in our current investigation (Figure 9d) [*Li et al.*, 2014].

Governed by the same multiphase reactive transport dynamics as binary metal alloys, the horizontally solidifying ice-brine systems explored in this work exhibit strikingly similar physicochemical characteristics (e.g., the formation of inverted A-segregates) and zonation trends (both lateral and vertical) to their magmatic and metallurgic analogs. The consistency between the ultimate physicochemical profiles of these systems, as well as the fundamental nature of the physics driving their evolution, suggests that chemical zonation, macrosegragation, and physicochemical heterogeneities introduced by variations in solidification geometry likely play a significant role in dictating the material properties and characteristics of ocean- and brine-derived ices formed at ‘nontraditional’ interfaces (geometries other than top-down planar solidification).

The potential for resolidifying hydrological features (lenses, fractures, dikes, etc.) to provide a mechanism that can introduce both lateral and vertical physicochemical heterogeneities into planetary ice shells has far reaching implications. We have demonstrated that the multiphase physics governing metallurgical and petrological solidification processes produce chemical zonation patterns and physicochemical heterogeneities that are mirrored by those observed in our simulations of planetary relevant ice-brine environments. In the former analog systems, the resulting macrosegregation and impurity distribution dictate characteristics of the resultant solids that influence global terrestrial geology and geophysics (e.g., magmatic differentiation) and are imperative to the strength, integrity, and durability of widely used industrially cast metals (e.g., building materials, tools, mechanical components) [*Campbell*, 2003; *Li et al.*, 2014; *Turcotte and Schubert*, 2014]. Similarly, segregation and solute distribution in ice-brine systems will influence the strength, rheology, dielectrics, melting point, permeability, and other material properties of planetary ices relevant to global ice shell geophysics (e.g., solid state convection, eutectic melting, fracture propagation/activity), transport capabilities (e.g., ocean-surface redox cycling, biosignature expression, brine mobilization), and observation via spacecraft (e.g., ice penetrating radar measurements). This is particularly pertinent to geologically active ice-ocean worlds such as Europa and Enceladus, that may possess contemporary near surface liquids [*Chivers et al.*, 2021; *Manga and Michaut*, 2017; *Michaut and Manga*, 2014; *Schmidt et al.*, 2011; *Walker et al.*, 2014] and active fractures that could be hydraulically connected to subsurface multiphase or liquid reservoirs [*Boury et al.*, 2021; *Postberg et al.*, 2009; *Postberg et al.*, 2011].

A particularly exciting result is the enhanced solute entrainment in lower portions of basal fractures due to the extended residence time of highly concentrated brine in the vertically elongated sidewall mushy layer as it percolates downward toward the ocean. This suggests that hydrologic and geophysical phenomenon capable of facilitating ice-brine interfaces whose normal vectors are not aligned with local gravity (fractures, dikes, sills, lenses) have the potential to retain more impurities than do planar interfaces formed via top-down solidification (e.g., [*Huppert*, 1990]). Furthermore, the degree to which impurity entrainment is amplified in these off-axis (nontraditional) interfaces is directly related to the vertical extant, or residence time of the downward percolating brine in, the mushy layer. Similarly, we hypothesize that the further the solidification interface deviates from the traditional top-down orientation (normal vector parallel to gravity – 0° deviation), the higher the level of potential impurity entrainment. This is consistent with the amplification of impurity entrainment in fractures with a normal vector perpendicular to gravity (90° deviation) and epitomized by the complete retention of impurities in the floors of lenses, whose normal vector is antiparallel to gravity (180° deviation). This is additionally supported by empirical observations of chemical zonation patterns in mushy layers grown at variable geometries [*Bédard et al.*, 1992; *Hebditch and Hunt*, 1974; *Huppert*, 1990; *Leitch*, 1987; *Stephen et al.*, 1987]. We note the specification of '*potential*' impurity entrainment, as we have also shown that for shallow fractures (~meters to tens of meters) the increase in efficiency of gravity drainage due to the horizontal freezing geometry results in *lower* impurity retention than in ice formed via top-down solidification subject to the same thermal forcing. Accordingly, we emphasize the additional complexities and competing dynamics introduced by nonstandard interface geometries. Nevertheless, given the putative efficiency of solute rejection at the contemporary ice-ocean interfaces of moons like Europa and Enceladus (due to low thermal gradients [*Wolfenbarger et al.*, 2019]) and the associated difficulty of introducing compositional heterogeneities into their overlying ice shells, the identification of a plausible geophysical mechanism that does just that is certainly significant. The mechanism's consistency with multiple macrosegragation and chemical zonation phenomena in terrestrial analog systems (magmatic, petrologic, metallurgic) provides a bolstered validation of the process at work and demonstrates the widespread occurrence and influence of reactive transport processes (e.g., [*Steefel et al.*, 2005]), giving further credence to the idea that it will likely be a prevalent process on icy worlds and have a substantial impact on the geophysical and biogeochemical evolution of planetary ice-ocean and ice-brine systems (e.g., fracture reactivation/propagation, material entrainment and transport across ice shells, ice shell hydrology, etc. [*Buffo et al.*, 2021b; *Vance et al.*, 2020]).

In the case of highly evolved fluids (e.g., brine that has been cryoconcentrated as it percolates through fracture walls or the last residual fluid in isolated sills) there is the potential for unique geochemical precipitates to occur. As brines reach their saturation or eutectic points the formation of a variety of salt hydrates will ensue (dependent on the brine's composition and local thermal environment), introducing additional novel phases into the ice shells of ocean worlds [*Durham et al.*, 2005; *McCarthy et al.*, 2007]. Both the sill and fracture geometries investigated here provide physical mechanisms that could facilitate cryoconcentration and precipitation of unique salt hydrates. While these phases would likely comprise only a small volumetric fraction of the ice shell, concentrated in regions associated with solidified/saturated hydrologic features, they would constitute unique cryopetrologic features containing deposits rich in non-ice geochemical species. Here we draw a potential analog to terrestrial pegmatites, the crystallization product of late-stage volatile-rich granitic magma [*Troch et al.*, 2021]. These intrusive pockets, dikes, and sills contain significant chemical zonation as well as some of the rarest Earth elements due to their unique enrichment in incompatible trace elements and late-stage solidification [*Thomas et al.*, 2006; *Troch et al.*, 2021]. In the ice-brine system, high salinity fluids may be additionally enriched in other impurities that cannot be incorporated into ice lattices, perhaps most notably organic or inorganic biosignatures. This concentrative effect could make such features lucrative targets for life detection missions that must contend with instrument sensitivity (detection limit) restrictions [*JPL*, 2017; *Schmidt*, 2020; *Schmidt and Buffo*, 2017]. Moreover, salt hydrates have been shown as a viable preservation medium for biosignatures, protecting them from radiation and oxidation [*Hays et al.*, 2017; *Perl et al.*, 2021; *Pontefract et al.*, 2019].

a

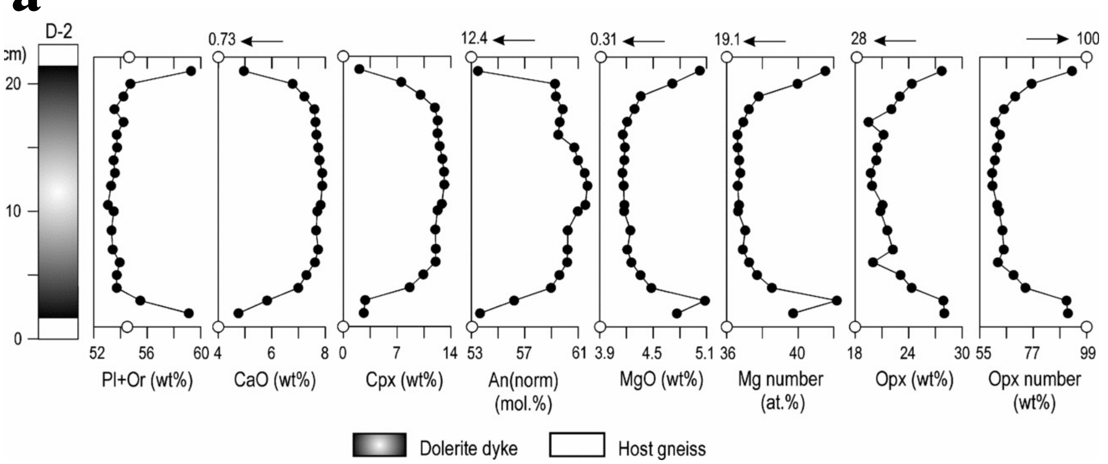

D-2
cm)
20
10
0
0.73
12.4
0.31
19.1
28
100
52 56 60
Pl+Or (wt%)
4 6 8
CaO (wt%)
0 7 14
Cpx (wt%)
53 57 61
An(norm) (mol.%)
3.9 4.5 5.1
MgO (wt%)
36 40 44
Mg number (at.%)
18 24 30
Opx (wt%)
55 77 99
Opx number (wt%)
Dolerite dyke
Host gneiss


b

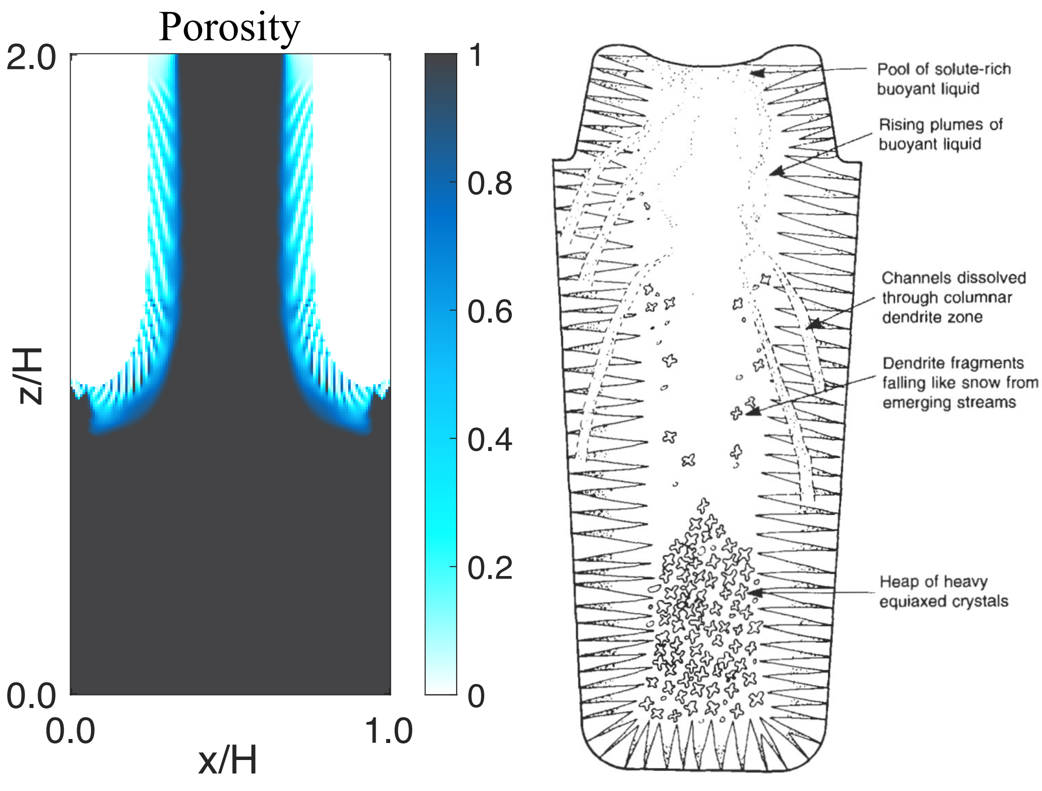

Porosity
2.0
0.0
z/H
0.0
1.0
x/H
1
0.8
0.6
0.4
0.2
0
Pool of solute-rich buoyant liquid
Rising plumes of buoyant liquid
Channels dissolved through columnar dendrite zone
Dendrite fragments falling like snow from emerging streams
Heap of heavy equiaxed crystals

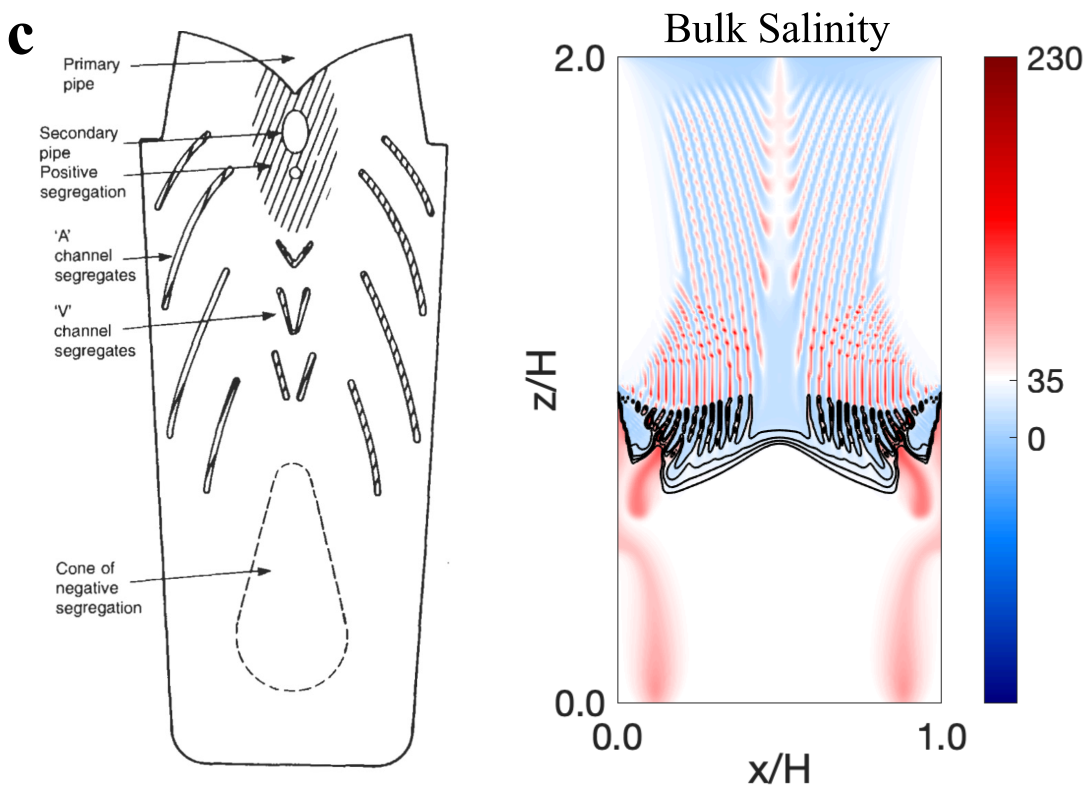
c
Primary pipe
Secondary pipe
Positive segregation
'A' channel segregates
'V' channel segregates
Cone of negative segregation
Bulk Salinity
2.0
0.0
z/H
0.0
1.0
x/H
230
35
0

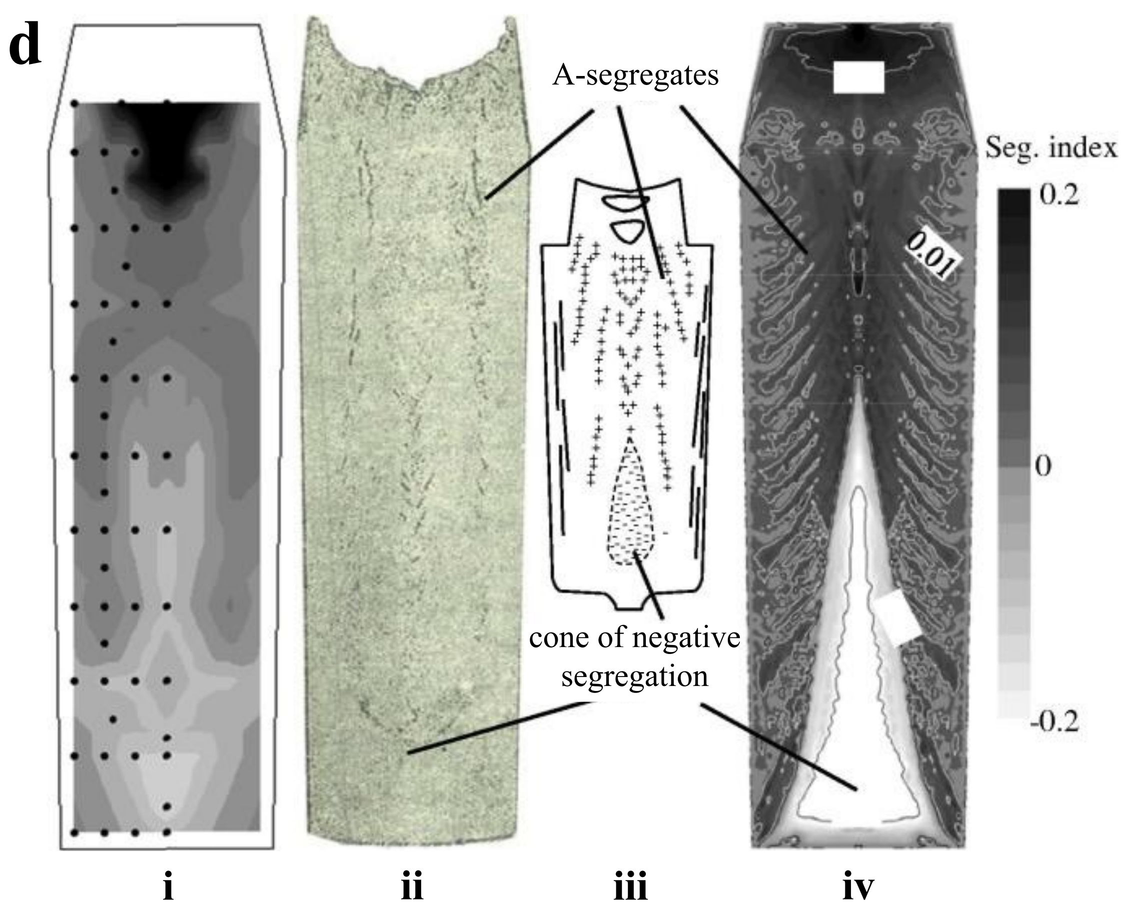
d
A-segregates
cone of negative segregation
Seg. index
0.2
0
-0.2
0.01
i
ii
iii
iv

943

**Figure 9** – Macrosegregation and chemical zonation trends in magmatic and metallurgic analog systems. **a)** Chemical zonation trends in a solidified dolerite dike [*Chistyakova and Latypov*, 2009]. Several components show edge to center depletion trends (normal fractionation) that mimic the salinity profiles of our simulated basal fractures (e.g., Figure 8e-f), while other component concentrations increase towards the center of the dike exhibiting 'reverse fractionation' tends. Such reverse fractionation trends, which do not follow from predicted liquidus phase equilibria, could add additional complexities to the resolidified systems and may have analogous counterparts in ice-brine systems (e.g., if certain ions could be preferentially incorporated into ice crystal lattices – clathrates). **b)** A depiction of the multiphase processes leading to A-segregate formation and chemical zonation during the solidification of metal alloy ingots (right, H = 1 m). The channels dissolving through the dendritic zone are akin to the brine channels formed in the mushy layer of basal fracture sidewalls (left). **c)** Impurity distribution patterns within a completely solidified metal alloy ingot (left). Note the structural similarities (e.g., diagonal geometry, distribution) between the A-segregates and the solidified brine channels of our simulated solidified basal fracture (right, H = 1 m). (right panel of 8b and left panel of 8c modified from [*Campbell*, 2003]) **d)** From Left to Right: **i)** Segregation map of a cast ingot, from [*Li et al.*, 2014], with black dots showing the location of drill samples. **ii)** Sulphur print of the same ingot. **iii)** Qualitative representation of the expected segregation pattern. **iv)** Numerical modelling prediction of segregation patterns in the same solidified ingot [*Li et al.*, 2014]. The consistency between the macrosegregation and chemical zonation patterns of their model and our results (e.g., channel and segregate formation, edge to center and vertical trends in impurity entrainment), coupled with the validation of their model against empirical measurements of cast ingot segregation and zonation patterns gives credence to our predictions of geometry-induced chemical heterogeneity, both fine scale channel formation and macroscale zonation, in solidifying ice-brine systems.

### 4.3 Applicability and Limitation of Analog Systems

The petrological, magmatic, and metallurgical processes highlighted in Section 4.1 and Section 4.2 suggest that comparable macrosegregation and multiphase reactive transport dynamics could be commonplace in planetary ices and have significant implications for the geophysics and habitability of ice-ocean worlds. However, it is important to assess the limitations of such comparisons and remain diligent in vetting the translation of system properties and/or dynamics lest we overprescribe such process similarities or overlook differences between high and low temperature multiphase systems. While the fundamental physics governing the solidification of metals, rocks, and aqueous solutions are the same there exist uniquities within each system that may differentiate their resultant dynamics, evolution, and material properties. As such, it is important to interpret and synthesize the implications of these analogisms for ice-ocean worlds with a critical acumen, armed with a knowledge of how ice-brine systems differ from their magmatic and metallurgic counterparts and how this may influence their multiphase evolution. Several publications have addressed the unique properties and behaviors of planetary ice-brine systems as well as the utility and limitations of utilizing terrestrial analog and numerical modeling approaches to improve our understanding of these exciting aqueous systems. *Buffo et al.* [2021b] specifically address the applicability and limitations of SOFTBALL, the model implemented in this investigation, and discuss precautious approaches to extending our contemporary state of knowledge regarding Earth-based ice-ocean/brine analogs to planetary environments. Other considerations are included in *Vance et al.* [2020], whose commentary of *Buffo et al.* [*2020*] highlighted the utility and limitations of terrestrial ice-ocean/brine and geophysical (e.g., magmatic, tectonic) analogs as well as contemporary multiphase reactive transport models and explored avenues and potential hurdles for future research, and *Schmidt* [2020], who provides a detailed discussion of the important links between geophysical processes, habitability, and biomarker production/preservation on ice-ocean worlds in the Jovian system.

Ultimately, laboratory investigations of bottom-up and lateral ice formation using our simulated ocean chemistries would be valuable benchmarks – similar to the investigations performed by *Leitch* [1987] for the aqueous sodium nitrate ($NaNO_3$) system and *Bédard et al.* [1992] for the aqueous ammonium chloride ($NH_4Cl$) system. These studies could be conducted in a manner akin to those of metal ingot characterization, wherein two-dimensional salinity profiles of an 'ice ingot' frozen via a controlled directional solidification would be measured – targeting thermal forcing such as bidirectional undercooling and vertical sidewall undercooling. The ability to control initial solution chemistry and thermal forcing in the lab would provide a method to investigate specific relationships between brine chemistry, thermal forcing, interface slope and resultant material entrainment. Furthermore, such experiments could either confirm or refute the formation of the inverted A-segregates and chemical zonation patterns predicted by our model. These type of laboratory measurements will be imperative to determining the validity of our use of metallurgic and magmatic analogs and will be crucial for quantifying and improving the accuracy of multiphase reactive transport models such as SOFTBALL. Given the importance of ice shell properties and dynamics to our understanding of multiple high-priority ice-ocean worlds, including Earth, these results and their byproducts will provide ground truthing resources for a significant portion of the planetary science and cryosphere communities. This is particularly true given the need to support and interpret the data from multiple upcoming missions to ocean worlds (JUICE, Dragonfly, Europa Clipper). As such, any targeted collaborative and cross-disciplinary efforts between the experimental and modeling communities to address these, and other similar, outstanding cryohydrologic questions/goals (e.g., permeability-porosity relationships in ocean/brine-derived ices [*Buffo et al.*, 2021b]) would be incredibly timely and pertinent to both planetary and Earth science research.

### 4.4 Future Outlooks

As the era of ocean world exploration accelerates (e.g., via missions such as Europa Clipper, JUICE, and Dragonfly) classification and quantification of ice-ocean world special regions will play a fundamental role in both planetary exploration (e.g., target identification) and planetary protection (e.g., contamination avoidance). Additionally, modeling techniques such as those presented here will be an indispensable tool for interpreting and synthesizing upcoming spacecraft observations of planetary ice shells. The ability to link the chemical fingerprints left by hydrological processes within ice shells to the thermophysical evolution of their progenitor fluid reservoirs will provide a powerful tool when paired with observational data such as ice penetrating radargrams. The significant dependance of ice penetrating radar on the dielectric properties of the substrate it is travelling through and the influence of both salts and brines on the dielectric properties of ice may provide a means to identify high salinity and/or aqueous environments within planetary ice shells and potentially characterize the nature (e.g., chemistry, habitability) and history of these environments. Finally, the versatility and adaptability of the SOFTBALL code will enable its ongoing application to our evolving understanding of ice-ocean world environments. The current investigation as well as other contemporary works [*Buffo et al.*, 2021b] have demonstrated the model's ability to accommodate new ocean/brine chemistries, planetary scales and environmental conditions, and more complex geometries and its adaptive architecture is primed to integrate additional system conditions and physics (e.g., geochemistry, biogeochemistry).

## 5 Conclusion

The chemically and geologically rich surfaces of many ice-ocean worlds in our solar system indicate that their ice shells are likely still active and that a host of putative geophysical processes could facilitate ocean-surface material transport essential for subsurface ocean habitability, driving geophysical processes, placing constraints on interior compositions, and the remote sensing of biosignatures. Given the difficulty of establishing fractures or conduits that penetrate the entire thickness of planetary ice shells – promoting direct ocean-surface exchange [*Rudolph and Manga*, 2009; *Walker et al.*, 2021] – the prevailing material transport theories invoke the notion that ocean materials will be entrained at the base of the ice shell via imperfect rejection at a multiphase ice-ocean interface [*Allu Peddinti and McNamara*, 2015; *Buffo et al.*, *2020; Buffo et al.*, 2021b]. These theories are supported by analogous observations of salt entrainment in terrestrial sea ice and congelation ice growth beneath ice shelves [*Cox and Weeks*, 1974; *Eicken*, 1992; *Notz et al.*, 2005; *Tison and Verbeke*, 2001; *Zotikov et al.*, 1980]. However, contemporary modeling and theoretical work has shown that the relatively shallow thermal gradients present at the base of planetary ice shells are such that only minimal levels of non-ice impurities will be entrained [*Buffo et al.*, *2020; Buffo et al.*, 2021b; *Hammond et al.*, 2018; *Wolfenbarger et al.*, 2018; *Wolfenbarger et al.*, 2019]. This is problematic for the ocean-surface transport rates needed to facilitate a chemically disequilibrated ocean favorable for metabolic reactions as well as several ice shell geophysical processes that may be driven by physicochemical heterogeneities within the ice [*Buffo et al.*, 2021b; *Vance et al.*, 2016; *Vance et al.*, 2020]. Accordingly, an additional mechanism beyond entrainment at a planar ice-ocean interface must be responsible for the incorporation and/or distribution of the observed chemical heterogeneities within planetary ice shells.

In the current study we demonstrated the potential for hypothesized hydrologic features within planetary ice shells (sills and basal fractures), which generate complex ice-ocean/brine interface geometries, to produce ice with higher levels of ocean/brine-derived impurities. We've shown that amplification of impurity entrainment is due to increased residence time of cryoconcentrated brine in the multiphase ice-brine interfacial layers that characterize the distal liquid-ice boundaries of these hydrologic features. The resolidifying walls of basal fractures retain vertically and horizontally heterogeneous levels of salt, as more concentrated brine from higher reaches of the fracture sidewall percolate through the interfacial mushy layer as it continues to freeze. The end member of this geometric effect is bottom-up freezing, such as what occurs at the floor of a lens or sill perched within the ice shell. In this case, no impurities are rejected from the ice as the freezing front propagates, retaining an exceptional chemical fingerprint of the parent fluid from whence the ice formed. *This geometrically influenced material entrainment amplification provides a potential solution to the problem of introducing chemical, and possibly biological, heterogeneities into planetary ice shells that would otherwise struggle to do so.*

The multiphase dynamics and resultant physicochemical trends exhibited by the ice-ocean/brine systems explored in this work closely mirror those of analogous magmatic, petrologic, and metallurgic systems on Earth – at both the small and large scale. The formation of diagonal brine channels and salt-rich macrosegregation patterns during fracture wall solidification is consistent with A-segregate formation in metal alloys and the horizontal and vertical bulk salinity trends of solidified fractures and sills mirror the chemical zonation patterns of solidified magmatic dikes, magma chambers, and multicomponent metal alloy castings. The broad and multiscale agreement between the properties of these disparate multiphase systems demonstrates the importance of multiphase reactive transport processes in governing the evolution of multiple planetary geophysical systems and lends credence to our results.

Given the potential prevalence of diverse, multiphase, brine-rich environments in planetary ice shells (e.g., [*Vance et al.*, 2020]) and the significant impact heterogeneous reactive transport processes have on the material properties and dynamic evolution of the terrestrial cryosphere, as well as petrologic, magmatic, and metallurgical analog systems, it stands to reason that inclusion of these physics in predictive models of ice-ocean worlds will move our understanding of these systems forward. Multiphase reactive transport models have revolutionized our conception of terrestrial geophysics and biogeochemistry, and their extension to icy worlds has already provided us with novel insights into the physicochemical structure and evolution of planetary ice shells [*Buffo et al.*, *2020; Buffo et al.*, 2021b; *Chivers et al.*, 2021; *Hammond et al.*, 2018; *Hesse et al.*, 2019; *Kalousová et al.*, 2018; *Kalousová et al.*, 2014; 2016; *Vance et al.*, 2020]. Coupling this knowledge with our current findings, that the multiphase solidification of geometrically complex ocean/brine filled hydrological features within planetary ice shells:

1) Provides a physical mechanism for amplified entrainment of ocean/brine-derived impurities into forming ice, particularly when compared to the low entrainment rates of a slowly solidifying or equilibrated planar ice-ocean interface.
2) Provides a physical mechanism for heterogeneous entrainment of ocean/brine-derived impurities into forming ice – a process lauded as integral for multiple ice shell geophysical processes and ocean-surface material transport.
3) Provides a physical mechanism for the cryoconcentration of non-ice impurities (e.g., salts, organics, etc.) that could introduce novel and localized deposits of salt hydrates and/or other eutectic mixtures (regions with fundamentally unique material properties) and facilitate the localization/concentration of astrobiologically relevant materials (e.g., nutrients, biosignatures) – processes important for ice shell geophysics, habitability, and biosignature expression.

suggests that planetary ice shells will be characterized by heterogeneous geologically, thermophysically, geochemically, and potentially biologically complex and dynamic environments. Given the astrobiological potential of diverse ocean worlds [*Des Marais et al.*, 2008; *Hendrix et al.*, 2019], and the fundamental role ice shell processes likely play in governing the geophysical evolution, habitability, and future exploration of these bodies (e.g., site selection, instrument detection limits, planetary protection, measurement interpretation) [*Buffo et al.*, *2020; Buffo et al.*, 2021b; *Kalousova et al.*, 2017; *Schroeder et al.*, 2016; *Vance et al.*, 2016; *Vance et al.*, 2020], it is imperative that our conception of planetary ice shells reflects this complexity and that future investigations – numerical, experimental, and analog – target the quantitative constraint and holistic understanding of multiphase ice-ocean/brine processes.

## 6 Data Availability

SOFTBALL and its associated documentation can be found in *Parkinson et al.* [2020a] and *Parkinson et al.* [2020b]. All model input files used in this manuscript can be found in the repository directory "mushy-layer/examples/lenses-fractures" [*Parkinson et al.*, 2020a].

## 7 Acknowledgements

The authors sincerely thank Dr. Jamie Parkinson, designer of SOFTBALL, for his continued support in our adaption and implementation of the model. Jacob Buffo and Colin Meyer were supported by the NASA Solar System Workings grant 80NSSC21K1804 and the NASA Established Program to Stimulate Competitive Research grant 80NSSC21M0329.

**References**


Allu Peddinti, D., and A. K. McNamara (2015), Material transport across Europa's ice shell, *Geophysical Research Letters*, *42*(11), 4288-4293, doi:10.1002/2015GL063950.

Arnold, N. S., S. J. Conway, F. E. G. Butcher, and M. R. Balme (2019), Modeled Subglacial Water Flow Routing Supports Localized Intrusive Heating as a Possible Cause of Basal Melting of Mars' South Polar Ice Cap, *Journal of Geophysical Research-Planets*, *124*(8), 2101-2116, doi:10.1029/2019je006061.

Assur, A. (1958), Composition of sea ice and its tensile strength, *Arctic sea ice*, *598*, 106-138.

Barr, A. C., and W. B. McKinnon (2007), Convection in ice I shells and mantles with self-consistent grain size, *Journal of Geophysical Research: Planets*, *112*(E2), doi:10.1029/2006JE002781.

Bédard, J. H., R. C. Kerr, and M. A. Hallworth (1992), Porous sidewall and sloping floor crystallization experiments using a reactive mush: implications for the self-channelization of residual melts in cumulates, *Earth and planetary science letters*, *111*(2-4), 319-329.

Berton, M., E. Nathan, H. Karani, T. Girona, C. Huber, P. G. Williard, and J. Head (2020), Experimental investigations on the effects of dissolved gases on the freezing dynamics of ocean worlds, *Journal of Geophysical Research: Planets*, *125*(8), e2020JE006528.

Boury, S., C. Meyer, G. Vasil, and A. Wells (2021), Convection in a mushy layer along a vertical heated wall, *Journal of Fluid Mechanics*, *926*.

Bryson, F. E., M. Nassif, P. A. Szot, C. J. Chivers, N. Daniel, B. E. Wiley, T. Plattner, A. Hanna, Y. Tomar, and S. Rapoport (2020), Vertical Entry Robot for Navigating Europa (VERNE) Mission and System Design, in *ASCEND 2020*, edited, p. 4061.

Buffo, J., et al. (2022), The Bioburden and Ionic Composition of Hypersaline Lake Ices: Novel Habitats on Earth and Their Astrobiological Implications, *Astrobiology*.

Buffo, J., B. Schmidt, C. Huber, and C. Meyer (2021a), Characterizing the Ice-Ocean Interface of Icy Worlds: A Theoretical Approach, *Icarus*.

Buffo, J., B. Schmidt, C. Huber, and C. Walker (*2020*), Entrainment and dynamics of ocean-derived impurities within Europa’s ice shell, *JGR: Planets*.

Buffo, J. J. (2019), Multiphase reactive transport in planetary ices, Georgia Institute of Technology.

Buffo, J. J., C. R. Meyer, J. R. Parkinson, and B. E. Schmidt (2021b), Dynamics of a solidifying icy satellite shell, *JGR: Planets*.

Campbell, J. (2003), *Castings*, Elsevier.

Carr, M. H., et al. (1998), Evidence for a subsurface ocean on Europa, *Nature*, *391*(6665), 363-365, doi:10.1038/34857.

Chistyakova, S., and R. Latypov (2009), Fine-scale chemical zonation in small mafic dykes, Kestiö Island, SW Finland, *Geological Magazine*, *146*(4), 485-496.

Chistyakova, S., and R. Latypov (2010), On the development of internal chemical zonation in small mafic dykes, *Geological Magazine*, *147*(1), 1-12, doi:10.1017/S0016756809990343.

Chivers, C., J. Buffo, and B. Schmidt (2021), Thermal and Chemical Evolution of Small, Shallow Water Bodies on Europa, *JGR: Planets*(2326), 1047.

Cosciotti, B., A. Balbi, A. Ceccarelli, C. Fagliarone, E. Mattei, S. E. Lauro, F. Di Paolo, E. Pettinelli, and D. Billi (2019), Survivability of Anhydrobiotic Cyanobacteria in Salty Ice: Implications for the Habitability of Icy Worlds, *Life (Basel)*, *9*(4), 86, doi:10.3390/life9040086.

Cottier, F., H. Eicken, and P. Wadhams (1999), Linkages between salinity and brine channel distribution in young sea ice, *Journal of Geophysical Research-Oceans*, *104*(C7), 15859-15871, doi:Doi 10.1029/1999jc900128.

Council, N. R. (2012), *Assessment of Planetary Protection Requirements for Spacecraft Missions to Icy Solar System Bodies*, National Academies Press.

Cox, G. F., and W. F. Weeks (1974), Salinity variations in sea ice, *Journal of Glaciology*, *13*(67), 109-120.

Craft, K. L., G. W. Patterson, R. P. Lowell, and L. Germanovich (2016), Fracturing and flow: Investigations on the formation of shallow water sills on Europa, *Icarus*, *274*, 297-313, doi:10.1016/j.icarus.2016.01.023.

Craven, M., I. Allison, H. A. Fricker, and R. Warner (2009), Properties of a marine ice layer under the Amery Ice Shelf, East Antarctica, *Journal of Glaciology*, *55*(192), 717-728, doi:Doi 10.3189/002214309789470941.

Culha, C., D. M. Schroeder, T. M. Jordan, and M. S. Haynes (2020), Assessing the detectability of Europa's eutectic zone using radar sounding, *Icarus*, *339*, 113578.

Des Marais, D. J., et al. (2008), The NASA Astrobiology Roadmap, *Astrobiology*, *8*(4), 715-730, doi:10.1089/ast.2008.0819.

Dombard, A. J., G. W. Patterson, A. P. Lederer, and L. M. Prockter (2013), Flanking fractures and the formation of double ridges on Europa, *Icarus*, *223*(1), 74-81, doi:10.1016/j.icarus.2012.11.021.

Durham, W. B., L. A. Stern, T. Kubo, and S. H. Kirby (2005), Flow strength of highly hydrated Mg-and Na-sulfate hydrate salts, pure and in mixtures with water ice, with application to Europa, *Journal of Geophysical Research: Planets*, *110*(E12).

Eicken, H. (1992), Salinity Profiles of Antarctic Sea Ice - Field Data and Model Results, *Journal of Geophysical Research-Oceans*, *97*(C10), 15545-15557, doi:Doi 10.1029/92jc01588.

Fagents, S. A., R. Greeley, R. J. Sullivan, R. T. Pappalardo, L. M. Prockter, and G. S. Team (2000), Cryomagmatic mechanisms for the formation of Rhadamanthys linea, triple band margins, and other low-albedo features on Europa, *Icarus*, *144*(1), 54-88, doi:DOI 10.1006/icar.1999.6254.

Feltham, D. L., N. Untersteiner, J. S. Wettlaufer, and M. G. Worster (2006), Sea ice is a mushy layer, *Geophysical Research Letters*, *33*(14), doi:Artn L14501
10.1029/2006gl026290.

Figueredo, P. H., and R. Greeley (2004), Resurfacing history of Europa from pole-to-pole geological mapping, *Icarus*, *167*(2), 287-+, doi:10.1016/j.icarus.2003.09.016.

Fowler, A. (1987), Theories of mushy zones: applications to alloy solidification, magma transport, frost heave and igneous intrusions, in *Structure and Dynamics of Partially Solidified Systems*, edited, pp. 159-199, Springer.

Fox-Powell, M. G., and C. S. Cockell (2018), Building a Geochemical View of Microbial Salt Tolerance: Halophilic Adaptation of Marinococcus in a Natural Magnesium Sulfate Brine, *Front Microbiol*, *9*, 739, doi:10.3389/fmicb.2018.00739.

Fox-Powell, M. G., J. E. Hallsworth, C. R. Cousins, and C. S. Cockell (2016), Ionic Strength Is a Barrier to the Habitability of Mars, *Astrobiology*, *16*(6), 427-442, doi:10.1089/ast.2015.1432.

Fricker, H. A., S. Popov, I. Allison, and N. Young (2001), Distribution of marine ice beneath the Amery Ice Shelf, *Geophysical Research Letters*, *28*(11), 2241-2244, doi:Doi 10.1029/2000gl012461.

Galton-Fenzi, B., J. Hunter, R. Coleman, S. Marsland, and R. Warner (2012), Modeling the basal melting and marine ice accretion of the Amery Ice Shelf, *Journal of Geophysical Research: Oceans*, *117*(C9).

Gleeson, D. F., R. T. Pappalardo, M. S. Anderson, S. E. Grasby, R. E. Mielke, K. E. Wright, and A. S. Templeton (2012), Biosignature Detection at an Arctic Analog to Europa, *Astrobiology*, *12*(2), 135-150, doi:10.1089/ast.2010.0579.

Greenberg, R., G. V. Hoppa, B. R. Tufts, P. Geissler, and J. Riley (1999), Chaos on Europa, *Icarus*, *141*(2), 263-286, doi:DOI 10.1006/icar.1999.6187.

Griewank, P. J., and D. Notz (2013), Insights into brine dynamics and sea ice desalination from a 1-D model study of gravity drainage, *Journal of Geophysical Research: Oceans*, *118*(7), 3370-3386.

Hallsworth, J. E., et al. (2007), Limits of life in MgCl2-containing environments: chaotropicity defines the window, *Environ Microbiol*, *9*(3), 801-813, doi:10.1111/j.1462-2920.2006.01212.x.

Hammond, N. P., E. Parmenteir, and A. C. Barr (2018), Compaction and Melt Transport in Ammonia-Rich Ice Shells: Implications for the Evolution of Triton, *Journal of Geophysical Research: Planets*, *123*(12), 3105-3118.

Han, L., and A. P. Showman (2005), Thermo-compositional convection in Europa's icy shell with salinity, *Geophysical research letters*, *32*(20).

Hays, L. E., H. V. Graham, D. J. Des Marais, E. M. Hausrath, B. Horgan, T. M. McCollom, M. N. Parenteau, S. L. Potter-McIntyre, A. J. Williams, and K. L. Lynch (2017), Biosignature preservation and detection in Mars analog environments, *Astrobiology*, *17*(4), 363-400.

Head, J., R. Pappalardo, R. Greeley, R. Sullivan, C. Pilcher, G. Schubert, W. Moore, M. Carr, J. Moore, and M. Belton (1997), Evidence for recent solid-state convection on Europa: The nature of pits, domes, spots, and ridges, paper presented at Bulletin of the American Astronomical Society.

Hebditch, D., and J. Hunt (1974), Observations of ingot macrosegregation on model systems, *Metallurgical transactions*, *5*(7), 1557-1564.

Helfenstein, P., and E. M. Parmentier (1983), Patterns of Fracture and Tidal Stresses on Europa, *Icarus*, *53*(3), 415-430, doi:Doi 10.1016/0019-1035(83)90206-3.

Hendrix, A. R., et al. (2019), The NASA Roadmap to Ocean Worlds, *Astrobiology*, *19*(1), 1-27, doi:10.1089/ast.2018.1955.

Hesse, M., J. Jordan, S. Vance, and C. McCarthy (2019), Oxidant Transport Through Europa's Ice Shell by Porosity Waves, paper presented at Lunar and Planetary Science Conference.

Hesse, M. A., and J. C. Castillo-Rogez (2019), Thermal Evolution of the Impact-Induced Cryomagma Chamber Beneath Occator Crater on Ceres, *Geophysical Research Letters*, *46*(3), 1213-1221, doi:10.1029/2018gl080327.

Holland, P. R., H. F. J. Corr, D. G. Vaughan, A. Jenkins, and P. Skvarca (2009), Marine ice in Larsen Ice Shelf, *Geophysical Research Letters*, *36*(11), doi:Artn L11604
10.1029/2009gl038162.

Hoppa, G., R. Greenberg, B. R. Tufts, P. Geissler, C. Phillips, and M. Milazzo (2000), Distribution of strike-slip faults on Europa, *Journal of Geophysical Research: Planets*, *105*(E9), 22617-22627.

Hoppa, G., B. R. Tufts, R. Greenberg, and P. Geissler (1999), Strike-slip faults on Europa: Global shear patterns driven by tidal stress, *Icarus*, *141*(2), 287-298, doi:DOI 10.1006/icar.1999.6185.

Howell, S. M., and R. T. Pappalardo (2018), Band Formation and Ocean-Surface Interaction on Europa and Ganymede, *Geophysical Research Letters*, *45*(10), 4701-4709.

Hunke, E. C., D. Notz, A. K. Turner, and M. Vancoppenolle (2011), The multiphase physics of sea ice: a review for model developers, *Cryosphere*, *5*(4), 989-1009, doi:10.5194/tc-5-989-2011.

Huppert, H. E. (1990), The fluid mechanics of solidification, *Journal of Fluid Mechanics*, *212*, 209-240.

Johnson, B. C., R. Y. Sheppard, A. C. Pascuzzo, E. A. Fisher, and S. E. Wiggins (2017), Porosity and Salt Content Determine if Subduction Can Occur in Europa's Ice Shell, *Journal of Geophysical Research-Planets*, *122*(12), 2765-2778, doi:10.1002/2017je005370.

JPL (2017), Report of the Europa Lander Science Definition Team.

Kalousova, K., D. M. Schroeder, and K. M. Soderlund (2017), Radar attenuation in Europa's ice shell: Obstacles and opportunities for constraining the shell thickness and its thermal structure, *Journal of Geophysical Research-Planets*, *122*(3), 524-545, doi:10.1002/2016je005110.

Kalousová, K., and C. Sotin (2020), Dynamics of Titan's high-pressure ice layer, *Earth and Planetary Science Letters*, *545*, 116416.

Kalousová, K., C. Sotin, G. Choblet, G. Tobie, and O. Grasset (2018), Two-phase convection in Ganymede's high-pressure ice layer—Implications for its geological evolution, *Icarus*, *299*, 133-147.

Kalousová, K., O. Souček, G. Tobie, G. Choblet, and O. Čadek (2014), Ice melting and downward transport of meltwater by two-phase flow in Europa's ice shell, *Journal of Geophysical Research: Planets*, *119*(3), 532-549.

Kalousová, K., O. Souček, G. Tobie, G. Choblet, and O. Čadek (2016), Water generation and transport below Europa's strike-slip faults, *Journal of Geophysical Research: Planets*, *121*(12), 2444-2462.

Khazendar, A., and A. Jenkins (2003), A model of marine ice formation within Antarctic ice shelf rifts, *Journal of Geophysical Research-Oceans*, *108*(C7), doi:Artn 3235
10.1029/2002jc001673.

Khazendar, A., E. Rignot, and E. Larour (2009), Roles of marine ice, rheology, and fracture in the flow and stability of the Brunt/Stancomb-Wills Ice Shelf, *Journal of Geophysical Research: Earth Surface*, *114*(F4).

Lawrence, J., B. Schmidt, P. Washam, C. L. Hulbe, H. J. Horgan, C. Stevens, G. B. Dunbar, M. R. Meister, B. Hurwitz, and E. Quartini (2020), ROV Icefin at Ross Ice Shelf Grounding Zone: 5 km of ice, ocean, seafloor, and crevasse exploration, paper presented at AGU Fall Meeting Abstracts.

Leitch, A. (1987), Various aqueous solutions crystallizing from the side, in *Structure and Dynamics of Partially Solidified Systems*, edited, pp. 37-57, Springer.

Leitch, A. M. (1985), Laboratory models of magma chambers evolving due to side-wall crystallization.

Li, J., M. Wu, A. Ludwig, and A. Kharicha (2014), Simulation of macrosegregation in a 2.45-ton steel ingot using a three-phase mixed columnar-equiaxed model, *International journal of heat and mass transfer*, *72*, 668-679.

Manga, M., and C. Michaut (2017), Formation of lenticulae on Europa by saucer-shaped sills, *Icarus*, *286*, 261-269, doi:10.1016/j.icarus.2016.10.009.

Manga, M., and A. Sinton (2004), Formation of bands and ridges on Europa by cyclic deformation: Insights from analogue wax experiments, *Journal of Geophysical Research-Planets*, *109*(E9), doi:Artn E09001 10.1029/2004je002249.

Manga, M., and C. Y. Wang (2007), Pressurized oceans and the eruption of liquid water on Europa and Enceladus, *Geophysical Research Letters*, *34*(7), doi:Artn L07202 10.1029/2007gl029297.

Matson, D. L., J. C. Castillo, J. Lunine, and T. V. Johnson (2007), Enceladus' plume: Compositional evidence for a hot interior, *Icarus*, *187*(2), 569-573, doi:10.1016/j.icarus.2006.10.016.

McCarthy, C., J. R. Blackford, and C. E. Jeffree (2013), Low-temperature-SEM study of dihedral angles in the ice-I/sulfuric acid partially molten system, *J Microsc*, *249*(2), 150-157, doi:10.1111/jmi.12003.

McCarthy, C., R. F. Cooper, D. L. Goldsby, W. B. Durham, and S. H. Kirby (2011), Transient and steady state creep response of ice I and magnesium sulfate hydrate eutectic aggregates, *Journal of Geophysical Research-Planets*, *116*(E4), doi:Artn E04007 10.1029/2010je003689.

McCarthy, C., R. F. Cooper, S. H. Kirby, K. D. Rieck, and L. A. Stern (2007), Solidification and microstructures of binary ice-I/hydrate eutectic aggregates, *American Mineralogist*, *92*(10), 1550-1560, doi:10.2138/am.2007.2435.

McGuinness, M. J., M. J. M. Williams, P. J. Langhorne, C. Purdie, and J. Crook (2009), Frazil deposition under growing sea ice, *Journal of Geophysical Research-Oceans*, *114*(C7), doi:Artn C07014 10.1029/2007jc004414.

Mehrabian, R., M. Keane, and M. Flemings (1970), Interdendritic fluid flow and macrosegregation; influence of gravity, *Metallurgical and Materials Transactions B*, *1*(5), 1209-1220.

Michaut, C., and M. Manga (2014), Domes, pits, and small chaos on Europa produced by water sills, *Journal of Geophysical Research: Planets*, *119*(3), 550-573.

Moore, J. C. (2000), Models of radar absorption in Europan ice, *Icarus*, *147*(1), 292-300, doi:DOI 10.1006/icar.2000.6425.

Nakawo, M., and N. K. Sinha (1981), Growth rate and salinity profile of first-year sea ice in the high Arctic, *Journal of Glaciology*, *27*(96), 315-330.

Nathan, E., M. Berton, T. Girona, H. Karani, C. Huber, J. Head III, and P. Williard (2019), The Freezing and Fracture of Icy Satellites: Experimental Analog and Stress Analysis, *AGUFM*, *2019*, P53D-3489.

Nimmo, F. (2020), Solving the puzzle of Enceladus's active south pole, *Proc Natl Acad Sci U S A*, *117*(28), 16107-16108, doi:10.1073/pnas.2011055117.

Nimmo, F., and E. Gaidos (2002), Strike-slip motion and double ridge formation on Europa, *Journal of Geophysical Research: Planets*, *107*(E4), 5-1-5-8.

Nimmo, F., and R. T. Pappalardo (2016), Ocean worlds in the outer solar system, *Journal of Geophysical Research-Planets*, *121*(8), 1378-1399, doi:10.1002/2016je005081.

Nimmo, F., and P. Schenk (2006), Normal faulting on Europa: implications for ice shell properties, *Journal of Structural Geology*, *28*(12), 2194-2203, doi:10.1016/j.jsg.2005.08.009.

Notz, D., J. S. Wettlaufer, and M. G. Worster (2005), A non-destructive method for measuring the salinity and solid fraction of growing sea ice in situ, *Journal of Glaciology*, *51*(172), 159-166, doi:Doi 10.3189/172756505781829548.

Notz, D., and M. G. Worster (2009), Desalination processes of sea ice revisited, *Journal of Geophysical Research-Oceans*, *114*(C5), doi:Artn C05006 10.1029/2008jc004885.

Pappalardo, R. T., and A. C. Barr (2004), The origin of domes on Europa: The role of thermally induced compositional diapirism, *Geophysical Research Letters*, *31*(1), doi:Artn L01701 10.1029/2003gl019202.

Parkinson, J. R. (2019), Nonlinear convection in sea ice and other mushy layers, 258 pp, University of Oxford.

Parkinson, J. R., D. F. Martin, and J. Buffo (2020a), jrgparkinson/mushy-layer: Code and input files for Europa simulations, edited, GitHub, doi:10.5281/zenodo.4118457.

Parkinson, J. R., D. F. Martin, A. J. Wells, and R. F. Katz (2020b), Modelling binary alloy solidification with adaptive mesh refinement, *Journal of Computational Physics: X*, *5*, 100043.

Perl, S., S. Adeli, C. Basu, B. K. Baxter, J. Bowman, E. Boyd, M. Cable, A. J. Celestian, C. S. Cockell, and F. A. Corsetti (2021), Salty Environments: The importance of evaporites and brine environments as habitats and preservers of biosignatures, *Bulletin of the American Astronomical Society*, *53*(4), 240.

Pontefract, A., C. E. Carr, and M. R. Osburn (2019), The Role of Ionic Composition and Concentration on Biosignature Preservation: Lessons from the “Spotted” Lakes of British Colombia, paper presented at 2019 Astrobiology Science Conference, AGU.

Postberg, F., S. Kempf, J. Schmidt, N. Brilliantov, A. Beinsen, B. Abel, U. Buck, and R. Srama (2009), Sodium salts in E-ring ice grains from an ocean below the surface of Enceladus, *Nature*, *459*(7250), 1098-1101, doi:10.1038/nature08046.

Postberg, F., J. Schmidt, J. Hillier, S. Kempf, and R. Srama (2011), A salt-water reservoir as the source of a compositionally stratified plume on Enceladus, *Nature*, *474*(7353), 620-622, doi:10.1038/nature10175.

Prockter, L. M., J. W. Head, R. T. Pappalardo, R. J. Sullivan, A. E. Clifton, B. Giese, R. Wagner, and G. Neukum (2002), Morphology of Europan bands at high resolution: A mid-ocean ridge-type rift mechanism, *Journal of Geophysical Research: Planets*, *107*(E5).

Quick, L. C., D. L. Buczkowski, O. Ruesch, J. E. C. Scully, J. Castillo-Rogez, C. A. Raymond, P. M. Schenk, H. G. Sizemor, and M. V. Sykes (2019), A Possible Brine Reservoir Beneath Occator Crater: Thermal and Compositional Evolution and Formation of the Cerealia Dome and Vinalia Faculae, *Icarus*, *320*, 119-135, doi:10.1016/j.icarus.2018.07.016.

Rudolph, M. L., and M. Manga (2009), Fracture penetration in planetary ice shells, *Icarus*, *199*(2), 536-541, doi:10.1016/j.icarus.2008.10.010.

Schmidt, B. (2020), The Astrobiology of Europa and the Jovian System, *Planetary Astrobiology*, 185.

Schmidt, B. E., D. D. Blankenship, G. W. Patterson, and P. M. Schenk (2011), Active formation of 'chaos terrain' over shallow subsurface water on Europa, *Nature*, *479*(7374), 502-505, doi:10.1038/nature10608.

Schmidt, B. E., and J. Buffo (2017), Biomarker Production and Preservation on Europa, paper presented at European Planetary Science Congress.

Schroeder, D. M., A. Romero-Wolf, L. Carrer, C. Grima, B. A. Campbell, W. Kofman, L. Bruzzone, and D. D. Blankenship (2016), Assessing the potential for passive radio sounding of Europa and Ganymede with RIME and REASON, *Planetary and Space Science*, *134*, 52-60, doi:10.1016/j.pss.2016.10.007.

Smedsrud, L. H., and A. Jenkins (2004), Frazil ice formation in an ice shelf water plume, *Journal of Geophysical Research-Oceans*, *109*(C3), doi:Artn C03025 10.1029/2003jc001851.

Sotin, C., J. W. Head, and G. Tobie (2002), Europa: Tidal heating of upwelling thermal plumes and the origin of lenticulae and chaos melting, *Geophysical Research Letters*, *29*(8), 74-71-74-74, doi:Artn 1233 10.1029/2001gl013844.

Sotin, C., and G. Tobie (2004), Internal structure and dynamics of the large icy satellites, *Comptes Rendus Physique*, *5*(7), 769-780, doi:10.1016/j.crhy.2004.08.001.

Sparks, W. B., K. P. Hand, M. A. McGrath, E. Bergeron, M. Cracraft, and S. E. Deustua (2016), Probing for Evidence of Plumes on Europa with Hst/Stis, *Astrophysical Journal*, *829*(2), 121, doi:Artn 121 10.3847/0004-637x/829/2/121.

Steefel, C. I., D. J. DePaolo, and P. C. Lichtner (2005), Reactive transport modeling: An essential tool and a new research approach for the Earth sciences, *Earth and Planetary Science Letters*, *240*(3-4), 539-558, doi:10.1016/j.epsl.2005.09.017.

Stephen, R., J. Sparks, and H. E. Huppert (1987), Laboratory Experiments with Aqueous Solutions Modelling Magma Chamber Processes. I. Discussion of Their Validity and Geological Application, in *Origins of Igneous Layering*, edited, pp. 527-538, Springer.

Thomas, R., J. D. Webster, and P. Davidson (2006), Understanding pegmatite formation: the melt and fluid inclusion approach, *Melt inclusions in plutonic rocks*, *36*, 189-210.

Tison, J.-L., and V. Verbeke (2001), Chlorinity/salinity distribution patterns in experimental granular sea ice, *Annals of Glaciology*, *33*, 13-20.

Toner, J. D., D. C. Catling, and B. Light (2014), The formation of supercooled brines, viscous liquids, and low-temperature perchlorate glasses in aqueous solutions relevant to Mars, *Icarus*, *233*, 36-47, doi:10.1016/j.icarus.2014.01.018.

Troch, J., C. Huber, and O. Bachmann (2021), The physical and chemical evolution of magmatic fluids in near-solidus silicic magma reservoirs: Implications for the formation of pegmatites, *Goldschmidt2021• Virtual• 4-9 July*.

Trumbo, S. K., M. E. Brown, and K. P. Hand (2019), Sodium chloride on the surface of Europa, *Sci Adv*, *5*(6), eaaw7123, doi:10.1126/sciadv.aaw7123.

Turcotte, D., and G. Schubert (2014), *Geodynamics*, Cambridge University Press.

Vance, S. D., K. P. Hand, and R. T. Pappalardo (2016), Geophysical controls of chemical disequilibria in Europa, *Geophysical Research Letters*, *43*(10), 4871-4879, doi:10.1002/2016gl068547.

Vance, S. D., B. Journaux, M. Hesse, and G. Steinbrügge (2020), The Salty Secrets of Icy Ocean Worlds, *Journal of Geophysical Research: Planets*, e2020JE006736.

Vance, S. D., M. P. Panning, S. Stähler, F. Cammarano, B. G. Bills, G. Tobie, S. Kamata, S. Kedar, C. Sotin, and W. T. Pike (2018), Geophysical investigations of habitability in ice-covered ocean worlds, *Journal of Geophysical Research: Planets*, *123*(1), 180-205.

Waite, J. H., Jr., et al. (2006), Cassini ion and neutral mass spectrometer: Enceladus plume composition and structure, *Science*, *311*(5766), 1419-1422, doi:10.1126/science.1121290.

Walker, C., and B. Schmidt (2015), Ice collapse over trapped water bodies on Enceladus and Europa, *Geophysical Research Letters*, *42*(3), 712-719.
Walker, C., B. Schmidt, and J. Bassis (2014), Breaking the ice: On the application of fracture system mechanics and fragmentation theory to the chaos regions of Europa, *LPI*(1777), 2659.
Walker, C. C., J. N. Bassis, and B. E. Schmidt (2021), Propagation of Vertical Fractures through Planetary Ice Shells: The Role of Basal Fractures at the Ice–Ocean Interface and Proximal Cracks, *The Planetary Science Journal*, *2*(4), 135.
Wells, A. J., J. R. Hitchen, and J. R. G. Parkinson (2019), Mushy-layer growth and convection, with application to sea ice, *Philos Trans A Math Phys Eng Sci*, *377*(2146), 20180165, doi:10.1098/rsta.2018.0165.
Wolfenbarger, N., D. Blankenship, K. Soderlund, D. Young, and C. Grima (2018), Leveraging Terrestrial Marine Ice Cores to Constrain the Composition of Ice on Europa, *LPI Contributions*, *2100*.
Wolfenbarger, N., K. Soderlund, and D. Blankenship (2019), Revisiting the Salt Distribution Coefficient for Icy Ocean Worlds, *LPI Contributions*, *2168*.
Worster, M. G., H. E. Huppert, and R. S. J. Sparks (1990), Convection and Crystallization in Magma Cooled from Above, *Earth and Planetary Science Letters*, *101*(1), 78-89, doi:Doi 10.1016/0012-821x(90)90126-I.
Worster, M. G., and D. W. Rees Jones (2015), Sea-ice thermodynamics and brine drainage, *Philos Trans A Math Phys Eng Sci*, *373*(2045), 20140166, doi:10.1098/rsta.2014.0166.
Zolotov, M. Y., and J. Kargel (2009), *On the chemical composition of Europa's icy shell, ocean, and underlying rocks*, University of Arizona Press Tucson, AZ.
Zotikov, I. A., V. S. Zagorodnov, and J. V. Raikovsky (1980), Core Drilling through the Ross Ice Shelf (Antarctica) Confirmed Basal Freezing, *Science*, *207*(4438), 1463-1464, doi:DOI 10.1126/science.207.4438.1463.

## Supporting Information template

Please use this template when formatting and submitting your Supporting Information.

This template serves as both a "table of contents" for the supporting information for your article and as a summary of files.

**Once you have completed this template, you should delete this instruction page.**

## Overview

Please note that all supporting information will be peer reviewed with your manuscript. For more information, please see the Supporting Information Guidelines in Author Resources

## Using this Template

Type or paste the appropriate text (title, author list, and corresponding authors) into the template below.

Contents of this document:

- All Supporting text and figures should be included in this document.
- Movie files and audio files should be uploaded separately, following AGU naming conventions. File name and descriptions for these should be included in this template.
- All references should be included in the reference list of the main paper so that they can be indexed, linked, and counted as citations. The reference section does not count toward length limits.

How to fill out this document:

- Insert supporting information content into each appropriate section of the template.
- Figures should appear above each caption.
- To add additional captions, simply copy and paste each sample caption as needed.
- You will be prompted to upload these files on the Upload Files tab during the submission process, using file type "Supporting Information (SI)"
- Data (displayed in tables) should only be shared in the Supporting Information section for the sole purpose of peer review.

*Journal of Geophysical Research: Planets*

Supporting Information for

# Geometry of Freezing Impacts Ice Composition: Implications for Icy Satellites

**J. J. Buffo[1], C. R. Meyer[1], C. J. Chivers[2, 3], C. C. Walker[3], C. Huber[4] and B. E. Schmidt[5]**

1 – Dartmouth College
2 – Georgia Institute of Technology
3 – Woods Hole Oceanographic Institution
4 – Brown University
5 – Cornell University

## Contents of this file

Text S1
Figures S1 to S2

## Additional Supporting Information (Files uploaded separately)

Captions for Movies M1 to M33

## Introduction

The following supplementary material contains an extended discussion of the multiphase evolution of the roofs and floors of sills simulated and discussed within the main manuscript and discusses the influence of reservoir chemistry and thermal driving on the thicknesses and propagation rates of these interfaces (Text S1). Figure S1 depicts the temporal evolution (growth) of sill floors and roofs during sill solidification. Figure S2 depicts the chemical evolution (salination) of the residual liquid reservoir during sill solidification. Captions for Movies M1-M33 describe the simulations these supporting .avi movies depict.

**Text S1 – Sill Roof and Floor Evolution**

During solidification the physicochemical properties and propagation rates of the multiphase 'mushy layers' that characterize the ice-brine interfaces of the roofs and floors of sills evolve. This evolution is dependent on the thermal gradients driving the solidification as well as the chemical composition of the sill. In Figure S1 we show the temporal evolution (growth) of the roof and floor mushy layers of the two sills (35 ppt NaCl and 35 ppt $MgSO_4$) we simulated in the main manuscript as well as the roof and floor mushy layer evolution of two additional sill simulations (1 – a freshwater (0 ppt) sill subject to the same thermal driving as the sills in the main manuscript and 2 – a 35 ppt NaCl sill with symmetric undercooling of 132 K at both the top and bottom boundary). These simulations were carried out to investigate the impacts environmental conditions (e.g., thermal driving, initial reservoir chemistry) have on mushy layer and sill roof/floor evolution. In three of the simulations, we track the ice-mush (IM) phase boundary as well as the mush-liquid (ML) phase boundary for both the roofs and floors of the sills. The space between these two phase boundaries defines the mushy layer – where a nonzero brine volume fraction exists. There does not exist a mushy layer in the freshwater sill (an expected result of freezing a pure fluid [*Huber et al.*, 2008; *Rubinšteĭn*, 2000]) so only the ML phase boundary is shown and represents a sharp ice-water transition.

Several expected trends are apparent in Figure S1 including 1) larger undercoolings lead to faster interface propagation; 2) floors have thicker mushy layers than roofs (consistent with our conclusions in the main manuscript); 3) mushy layers thin near the end of the sill solidifications as the residual fluid concentrates; and 4) mushy layers in $MgSO_4$ systems are much thinner than those of NaCl systems. Another less intuitive trend is also evident – the similar propagation rate of the freshwater sill roof and the ML interfaces of comparably undercooled saline sills, which sometimes even exceed the rate of the freshwater sill. While somewhat counterintuitive, given the freezing point depression effects of a saline/concentrating sill, ML interface propagation is primarily driven by conductive heat loss to the cold adjacent ice [*Buffo et al.*, 2021a], which can continue to be efficient in the ice phase of the mushy layer. Brine convection within the mushy layer may also amplify the efficiency of heat loss from the liquid reservoir, potentially explaining the ML propagation rates that exceed those of the freshwater roof. Interestingly, the ML interface propagation of the sill floor outpaces that of the sill roof in the symmetric undercooling case (dashed blue line and solid blue line of Figure S1, respectively). This suggests that while brine convection in the roof mushy layer amplifies heat loss from the residual reservoir it also acts to cycle relatively warm water into the roof mushy layer from the reservoir, slowing its ML interface propagation in relation to the floor ML interface.

In the end these comparative simulations show that both thermal driving and reservoir chemistry play a role in governing mushy layer thicknesses – shallower thermal gradients lead to thicker mushy layers and mushy layer thickness is proportional to the freezing point depression effects of solutes (i.e., NaCl results in thicker mushy layers as it has a much low eutectic temperature and saturation point). Conversely, while thermal driving plays a large role in governing mushy layer interface propagation rates (interface propagation rates are proportional to the magnitude of the driving thermal gradient) salinity plays a much smaller role and minimally impacts the rate of the ice-liquid/mush-liquid interface (additional tests with nonzero salinities distinct from the 35 ppt values used in the current simulations would need to be carried out to determine the effect of salinity on the propagation rates of the IM interface).

Environmental conditions (e.g., thermal environment, brine chemistry) have significant impacts on the structure, dynamics, and evolution of ice-brine interfaces on icy worlds throughout the solar system, including Earth [*Feltham et al.*, 2006; *Hunke et al.*, 2011]. Given the importance of these interfaces in governing the evolution of planetary ice shells and any internal hydrological features they may contain as well as their integral role in mediating material and heat transport between planetary hydrospheres and cryospheres [*Buffo et al.*, *2020; Vance et al.*, 2016; *Vance et al.*, 2020], constraining the physicochemical properties and dynamics of ice-brine mushy layers will play a fundamental role in improving our understanding and predictive modeling capabilities of ice-ocean world geophysics, habitability, and spacecraft mission observations (see discussions in *Buffo et al.* [2021b] and *Vance et al.* [2020]).

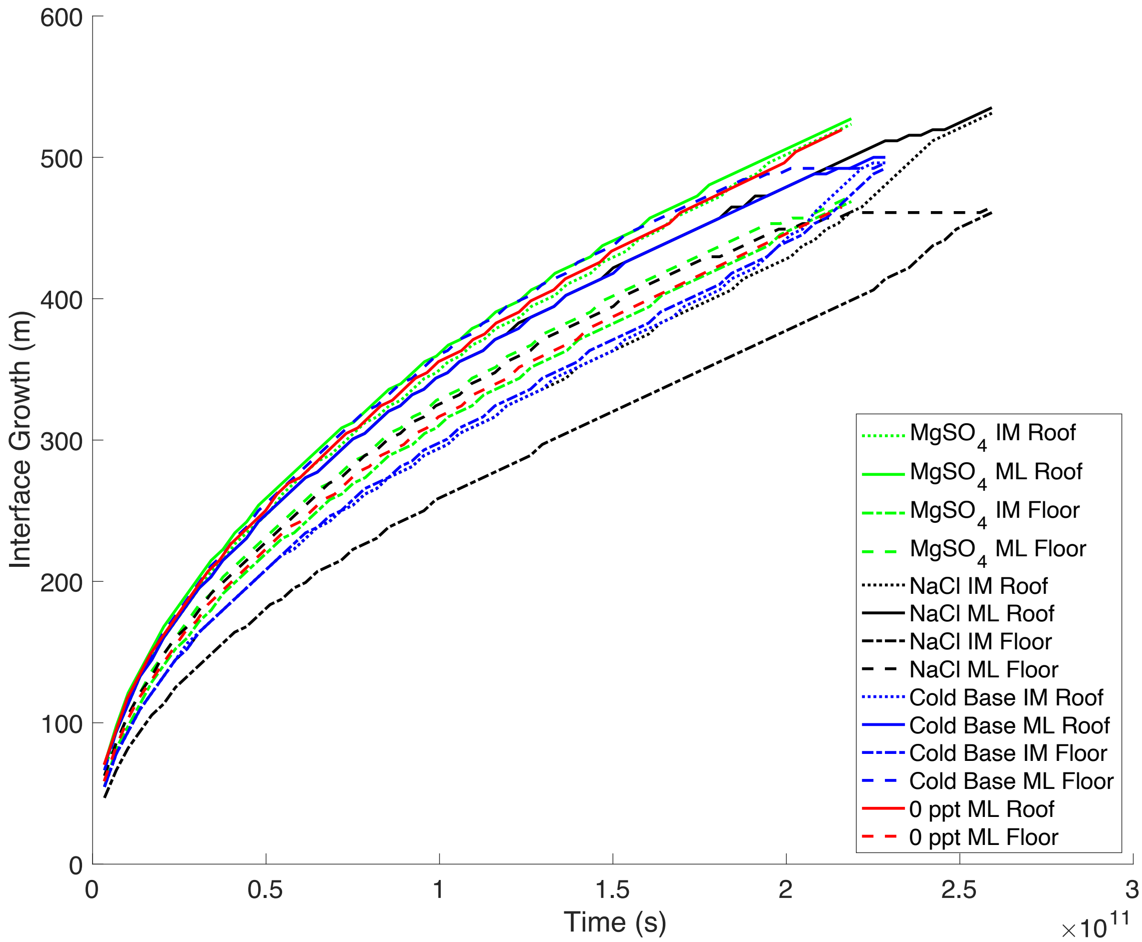


**Figure S1. The growth of sill floor and roof mushy layers.** The temporal propagation of the key interfaces that define the mushy layers of sill floors and roofs are plotted for all four simulations described in Text S1. Lines labeled as '$MgSO_4$' and 'NaCl' represent results from the 35 ppt sill simulations described in the main manuscript. Lines labeled as 'Cold Base' represent results from a 35 ppt NaCl sill solidification simulation driven by symmetric Dirichlet thermal forcing at its upper and lower boundaries of 132 K. Lines labeled as '0 ppt' represent results from the solidification of a freshwater sill subject to the same thermal forcing describe in the main manuscript. 'IM' signifies the ice-mush interface – the transition between a solid below the eutectic (porosity = 0) and the mushy layer (porosity >0), and 'ML' signifies the mush-liquid interface – the transition between the mushy layer and the reservoir fluid (porosity = 1).

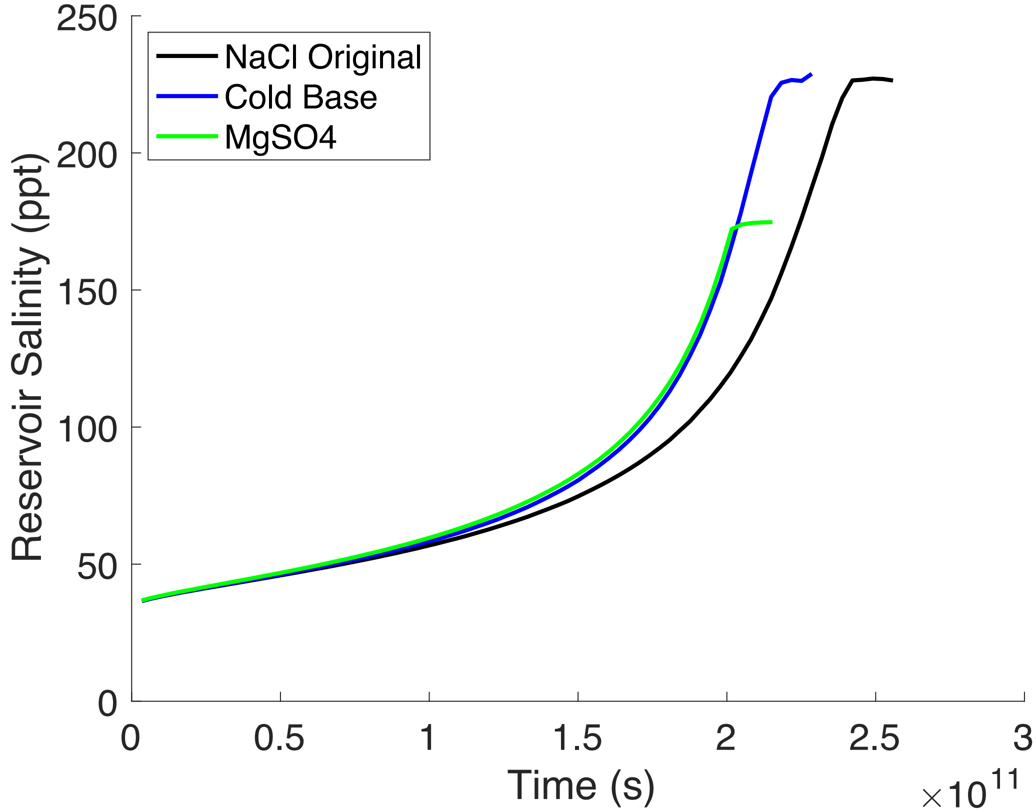


**Figure S2. Salination of solidifying sills.** As isolated sills freeze brine is rejected from the mushy layers of their roofs, concentrating their residual liquid reservoir. The temporal evolution of this process is shown for three different simulations. The plateaus near the end of the run correspond to the eutectic concentrations of the respective sills.

**Movie S1.** Bulk salinity evolution of a 1 km thick 35 ppt NaCl sill subject to the undercooling boundary conditions presented in Figure 2. Black contours demarcate porosities ranging from 0.15 to 0.95 in increments of 0.2.

**Movie S2.** Porosity evolution of a 1 km thick 35 ppt NaCl sill subject to the undercooling boundary conditions presented in Figure 2.

**Movie S3.** Streamline evolution of a 1 km thick 35 ppt NaCl sill subject to the undercooling boundary conditions presented in Figure 2. Streamlines are represented as blue to red contours that indicate relative flow speed along the streamline.

**Movie S4.** Bulk salinity evolution of a 1 km thick 35 ppt $MgSO_4$ sill subject to the undercooling boundary conditions presented in Figure 2. Black contours demarcate porosities ranging from 0.15 to 0.95 in increments of 0.2.

**Movie S5.** Porosity evolution of a 1 km thick 35 ppt $MgSO_4$ sill subject to the undercooling boundary conditions presented in Figure 2.

**Movie S6.** Streamline evolution of a 1 km thick 35 ppt $MgSO_4$ sill subject to the undercooling boundary conditions presented in Figure 2. Streamlines are represented as blue to red contours that indicate relative flow speed along the streamline.

**Movie S7.** Bulk salinity evolution of a 1 m by 1 m 35 ppt NaCl ocean filled fracture subject to the undercooling boundary conditions presented in Figure 2 (200 K undercooling). Black contours demarcate porosities ranging from 0.15 to 0.95 in increments of 0.2.

**Movie S8.** Porosity evolution of a 1 m by 1 m 35 ppt NaCl ocean filled fracture subject to the undercooling boundary conditions presented in Figure 2 (200 K undercooling).

**Movie S9.** Streamline evolution of a 1 m by 1 m 35 ppt NaCl ocean filled fracture subject to the undercooling boundary conditions presented in Figure 2 (200 K undercooling). Streamlines are represented as blue to red contours that indicate relative flow speed along the streamline.

**Movie S10.** Bulk salinity evolution of a 10 m by 20 m 35 ppt NaCl ocean filled fracture subject to the undercooling boundary conditions presented in Figure 2 (200 K undercooling). Black contours demarcate porosities ranging from 0.15 to 0.95 in increments of 0.2.

**Movie S11.** Porosity evolution of a 10 m by 20 m 35 ppt NaCl ocean filled fracture subject to the undercooling boundary conditions presented in Figure 2 (200 K undercooling).

**Movie S12.** Streamline evolution of a 10 m by 20 m 35 ppt NaCl ocean filled fracture subject to the undercooling boundary conditions presented in Figure 2 (200 K undercooling). Streamlines are represented as blue to red contours that indicate relative flow speed along the streamline.

**Movie S13.** Bulk salinity evolution of a 100 m by 200 m 35 ppt NaCl ocean filled fracture subject to the undercooling boundary conditions presented in Figure 2 (200 K undercooling). Black contours demarcate porosities ranging from 0.15 to 0.95 in increments of 0.2.

**Movie S14.** Porosity evolution of a 100 m by 200 m 35 ppt NaCl ocean filled fracture subject to the undercooling boundary conditions presented in Figure 2 (200 K undercooling).

**Movie S15.** Streamline evolution of a 100 m by 200 m 35 ppt NaCl ocean filled fracture subject to the undercooling boundary conditions presented in Figure 2 (200 K undercooling). Streamlines are represented as blue to red contours that indicate relative flow speed along the streamline.

**Movie S16.** Bulk salinity evolution of a 500 m by 1000 m 35 ppt NaCl ocean filled fracture subject to the undercooling boundary conditions presented in Figure 2 (200 K undercooling). Black contours demarcate porosities ranging from 0.15 to 0.95 in increments of 0.2.

**Movie S17.** Porosity evolution of a 500 m by 1000 m 35 ppt NaCl ocean filled fracture subject to the undercooling boundary conditions presented in Figure 2 (200 K undercooling).

**Movie S18.** Streamline evolution of a 500 m by 1000 m 35 ppt NaCl ocean filled fracture subject to the undercooling boundary conditions presented in Figure 2 (200 K undercooling). Streamlines are represented as blue to red contours that indicate relative flow speed along the streamline.

**Movie S19.** Bulk salinity evolution of a 1 m by 1 m 35 ppt $MgSO_4$ ocean filled fracture subject to the undercooling boundary conditions presented in Figure 2 (200 K undercooling). Black contours demarcate porosities ranging from 0.15 to 0.95 in increments of 0.2.

**Movie S20.** Porosity evolution of a 1 m by 1 m 35 ppt $MgSO_4$ ocean filled fracture subject to the undercooling boundary conditions presented in Figure 2 (200 K undercooling).

**Movie S21.** Streamline evolution of a 1 m by 1 m 35 ppt $MgSO_4$ ocean filled fracture subject to the undercooling boundary conditions presented in Figure 2 (200 K undercooling). Streamlines are represented as blue to red contours that indicate relative flow speed along the streamline.

**Movie S22.** Bulk salinity evolution of a 10 m by 20 m 35 ppt $MgSO_4$ ocean filled fracture subject to the undercooling boundary conditions presented in Figure 2 (200 K undercooling). Black contours demarcate porosities ranging from 0.15 to 0.95 in increments of 0.2.

**Movie S23.** Porosity evolution of a 10 m by 20 m 35 ppt $MgSO_4$ ocean filled fracture subject to the undercooling boundary conditions presented in Figure 2 (200 K undercooling).

**Movie S24.** Streamline evolution of a 10 m by 20 m 35 ppt $MgSO_4$ ocean filled fracture subject to the undercooling boundary conditions presented in Figure 2 (200 K undercooling). Streamlines are represented as blue to red contours that indicate relative flow speed along the streamline.

**Movie S25.** Bulk salinity evolution of a 100 m by 200 m 35 ppt $MgSO_4$ ocean filled fracture subject to the undercooling boundary conditions presented in Figure 2 (200 K undercooling). Black contours demarcate porosities ranging from 0.15 to 0.95 in increments of 0.2.

**Movie S26.** Porosity evolution of a 100 m by 200 m 35 ppt $MgSO_4$ ocean filled fracture subject to the undercooling boundary conditions presented in Figure 2 (200 K undercooling).

**Movie S27.** Streamline evolution of a 100 m by 200 m 35 ppt $MgSO_4$ ocean filled fracture subject to the undercooling boundary conditions presented in Figure 2 (200 K undercooling). Streamlines are represented as blue to red contours that indicate relative flow speed along the streamline.

**Movie S28.** Bulk salinity evolution of a 500 m by 1000 m 35 ppt $MgSO_4$ ocean filled fracture subject to the undercooling boundary conditions presented in Figure 2 (200 K undercooling). Black contours demarcate porosities ranging from 0.15 to 0.95 in increments of 0.2.

**Movie S29.** Porosity evolution of a 500 m by 1000 m 35 ppt $MgSO_4$ ocean filled fracture subject to the undercooling boundary conditions presented in Figure 2 (200 K undercooling).

**Movie S30.** Streamline evolution of a 500 m by 1000 m 35 ppt $MgSO_4$ ocean filled fracture subject to the undercooling boundary conditions presented in Figure 2 (200 K undercooling). Streamlines are represented as blue to red contours that indicate relative flow speed along the streamline.

**Movie S31.** Bulk salinity evolution of a 500 m by 1000 m 35 ppt NaCl ocean filled fracture subject to the undercooling boundary conditions presented in Figure 2 (260 K undercooling). Black contours demarcate porosities ranging from 0.15 to 0.95 in increments of 0.2.

**Movie S32.** Porosity evolution of a 500 m by 1000 m 35 ppt NaCl ocean filled fracture subject to the undercooling boundary conditions presented in Figure 2 (260 K undercooling).

**Movie S33.** Streamline evolution of a 500 m by 1000 m 35 ppt NaCl ocean filled fracture subject to the undercooling boundary conditions presented in Figure 2 (260 K undercooling). Streamlines are represented as blue to red contours that indicate relative flow speed along the streamline.

**References**


Buffo, J., B. Schmidt, C. Huber, and C. Meyer (2021a), Characterizing the Ice-Ocean Interface of Icy Worlds: A Theoretical Approach, *Icarus*.

Buffo, J., B. Schmidt, C. Huber, and C. Walker (*2020*), Entrainment and dynamics of ocean-derived impurities within Europa's ice shell, *JGR: Planets*.

Buffo, J. J., C. R. Meyer, J. R. Parkinson, and B. E. Schmidt (2021b), Dynamics of a solidifying icy satellite shell, *JGR: Planets*.

Feltham, D. L., N. Untersteiner, J. S. Wettlaufer, and M. G. Worster (2006), Sea ice is a mushy layer, *Geophysical Research Letters*, *33*(14), doi:Artn L14501
10.1029/2006gl026290.

Huber, C., A. Parmigiani, B. Chopard, M. Manga, and O. Bachmann (2008), Lattice Boltzmann model for melting with natural convection, *International Journal of Heat and Fluid Flow*, *29*(5), 1469-1480, doi:10.1016/j.ijheatfluidflow.2008.05.002.

Hunke, E. C., D. Notz, A. K. Turner, and M. Vancoppenolle (2011), The multiphase physics of sea ice: a review for model developers, *Cryosphere*, *5*(4), 989-1009, doi:10.5194/tc-5-989-2011.

Rubinšteĭn, L. (2000), *The stefan problem*, American Mathematical Soc.

Vance, S. D., K. P. Hand, and R. T. Pappalardo (2016), Geophysical controls of chemical disequilibria in Europa, *Geophysical Research Letters*, *43*(10), 4871-4879, doi:10.1002/2016gl068547.

Vance, S. D., B. Journaux, M. Hesse, and G. Steinbrügge (2020), The Salty Secrets of Icy Ocean Worlds, *Journal of Geophysical Research: Planets*, e2020JE006736.